# Rheo-PIV of yield-stress fluids in a 3D-printed fractal vane-in-cup geometry

Esteban F. Medina-Bañuelos and Benjamín M. Marín-Santibáñez

Escuela Superior de Ingeniería Química e Industrias Extractivas, Instituto Politécnico

Nacional, U. P. Adolfo López Mateos, C. P. 07738 Ciudad de México, México


Emad Chaparian

James Weir Fluid Laboratory, Department of Mechanical & Aerospace Engineering,

University of Strathclyde, Glasgow, United Kingdom


Crystal E. Owens and Gareth H. McKinley

Hatsopoulos Microfluids Laboratory, Department of Mechanical Engineering,

Massachusetts Institute of Technology; Massachusetts, USA


José Pérez-González*

Laboratorio de Reología y Física de la Materia Blanda, Escuela Superior de Física y

Matemáticas, Instituto Politécnico Nacional, U. P. Adolfo López Mateos, C. P. 07738

Ciudad de México, México


*Correspondence to:

Prof. José Pérez-González

E-mail: jpg@esfm.ipn.mx; jperezgo@ipn.mx

**ABSTRACT**

The vane-in-cup (VIC) geometry has been widely used for the rheological characterization of yield-stress fluids because it minimizes slip effects at the liquid/solid interface of the rotating geometry and reduces sample damage during the loading process. However, severe kinematic limitations arising from the spatial complexity of mixed shear and extensional flow have been identified for quantitative rheometrical measurements in complex fluids. Recently, vanes with fractal cross-sections have been suggested as alternatives for accurate rheometry of elastoviscoplastic fluids. In this work, the steady fractal vane-in-cup (fVIC) flow of a Newtonian fluid and a non-thixotropic Carbopol® 940 microgel, as well as the unsteady flow of a thixotropic κ-Carrageenan gel are analyzed using rheo-particle image velocimetry (Rheo-PIV). We describe the velocity distributions in all cases and show that the fVIC produces an almost axisymmetric flow field and rotation rate-independent 'effective radius' when used with both the Newtonian fluid and microgel. These findings enable the safe use of both the *Couette analogy* and the torque-stress conversion scheme for a 24-arm fVIC, as well as validate it as a reliable rheometrical tool for characterization of a variety of complex fluids. With the κ-Carrageenan gel, however, the axial shearing/compression while inserting the rheometric tool into the sample accelerates syneresis that results in shear banding for Couette and fVIC flows. By comparing results obtained using the 24-arm fVIC with other conventional geometries, we investigate the effect that the lateral and cross-sectional (shearing/compressing) area of the measuring fixture have on disrupting the κ-Carrageenan gel during its insertion.

## I. INTRODUCTION

The vane-in-cup (VIC) rheometer is a variant of the tangential annular (cylindrical Couette) flow that was originally developed for measurements of the shear strength of soils [1] and subsequently adopted for the characterization of elastoviscoplastic or yield-stress fluids, since it helps minimize the role of wall slip of the sample at the rotating geometry and limits the damage to shear-sensitive materials during sample loading or tool insertion [2, 3]. The VIC geometry consists of two components, namely, a cruciform vane (typically with 4, 6 or 8 evenly spaced blades) and a cylindrical cup. A torsional shearing flow is produced when the vane (with rigid unyielded sample filling the spaces between the blades) deforms the fluid in the annular space either under constant torque or constant rotational speed conditions.

The use of the VIC geometry as a rheometer is based on the so-called *Couette analogy*. To proceed with a kinematic analysis, the vane (with the fluid in-between the blades) is assumed to rotate as a single solid cylinder or rigid 'bob' with an equivalent radius, $R_{eq}$ [4-6], which is found, in general, to be slightly smaller than the actual vane radius, $R_V$ [7]. However, the shearing profile is generally not completely axisymmetric; there are stress singularities at each of the (thin) blade tips and the stress field in the fluid sample shows periodic spatial variations [8-10], which may lead to streamlines that are not perfectly circular. These observations have been corroborated by different authors who have visualized or simulated the shear zones and path lines for the VIC flow of different Newtonian and non-Newtonian fluids [3, 7, 10, 11-18]. Detailed observations of the velocity field show that the shearing surfaces adopt a locally polygonal structure close to the blades (with the number of vertices set by the number of blades) and gradually become increasingly cylindrical further away from the vane tips. The details of this transition

depend on the rheological characteristics of the fluid. The overall flow field is thus not viscometric since rigid body-like regions, as well as locally shear-dominated and extension-dominated regions are present for the fluid near the rotating blades [3, 7, 15-18]. Most importantly, the azimuthal variation of the yield surface or the set of radial positions at which the maximum tangential velocity, $V_{\theta max}$, occurs is found to change with the imposed torque, which impedes *a priori* determination of $R_{eq}$ to apply the *Couette analogy* for a given VIC configuration. Despite these drawbacks, it is fair to say that the VIC geometry can be a useful tool for rheological characterization of elastoviscoplastic fluids provided that knowledge of the flow kinematics is available from independent measurements to calculate the true shear rate in the gap [7].

Recently, Owens *et al.* [19] introduced a new class of 3D-printed vane fixtures with non-standard cross sections, i.e., non-bladed vanes in order to improve the accuracy of rheological measurements of Newtonian and shear-thinning fluids as well as yield-stress materials. These bespoke vanes include designs with fractal and gear-type cross-sectional planforms, designed with the goal of reducing recirculation of fluid in-between the blades and increasing the azimuthal stress homogeneity in the sample without enlarging the occluded area fraction (OAF). This parameter is related to the transverse sectional area of the rigid vane fixture and large values (e.g. a cylindrical Couette bob has an OAF = 1) can disrupt and damage shear-sensitive samples during immersion. Owens *et al*. used their vane fixtures to test a series of fluids, including a Newtonian fluid, a non-thixotropic yield-stress fluid (Carbopol®), a thixotropic yield-stress material (mayonnaise), and a carbon black-based battery slurry. In place of using the *Couette analogy*, these authors first obtained an expression to calculate the effective shear rate at the edge of the vane from the imposed rotation rate. Then they simulated the stress field around the vane tips for a Newtonian fluid

and showed that increasing the number of vane arms makes the stress field tend to that expected for a cylindrical bob, i.e., a homogeneous azimuthal shear stress distribution. Finally, they developed a conversion factor between the measured torque and the shear stress for an arbitrary N-arm vane (approximately incorporating end effects). Excellent agreement with benchmark measurements obtained using a cone-plate reference geometry was obtained for both Newtonian and elastoviscoplastic fluids using a 24-arm fractal vane. More recently, Carraretto *et al*. [20] used a 4-blade VIC and a 12-arm fVIC geometry to study various evolving coarsening foams with low liquid-phase volume fraction (gas fraction $85 \leq \phi \leq 99$). The 12-arm fVIC rheological measurements along with the conversion factor for the shear stress [19] allowed the authors to model the evolution of linear viscoelastic and shear flow behaviors of the foams by constructing rheological master curves.

Despite the obvious immediate practical benefits that the introduction of the bespoke 3D-printed vanes may represent for rheological characterization of complex fluids [19, 20], it is noteworthy that the results and conclusions are based purely on mechanical measurements. So, there are still some issues that need to be addressed regarding validation of the assumed flow field and performance of these fractal vane-in-cup (fVIC) geometries in more demanding situations, namely, when analyzing more complex fluids, such as thixotropic and shear banding fluids. Chaparian *et al.* [18] have pointed out the relevance that detailed determination of the local kinematics with high spatial resolution may represent for optimizing the design and reproducibility in measurements of the rheological behavior of viscoplastic fluids using this type of vane geometries. This led Chaparian *et al.* to carry out a computational analysis to assess the homogeneity of the stress and velocity fields around conventional or "standard" geometries and compare the results with those

obtained using fVIC geometries for ideal viscoplastic fluids modeled by the Bingham and Herschel-Bulkley constitutive equations, with and without wall slip. Detailed analysis showed that markedly improved spatial homogeneity in both velocity and stress fields was obtained with fractal vane designs, but they were not able to validate the kinematic predictions due to the absence of any measurements of the local velocity field. Thus, in the present study, we have addressed the problem of determining the flow kinematics near a 3D-printed fVIC geometry for fluids with different degrees of complexity. A rheo-PIV analysis is performed for flow around a 24-arm fractal vane of a Newtonian fluid (glycerol), a non-thixotropic yield-stress fluid, that is, a *0.12 wt.%* poly(acrylic acid) (Carbopol® 940) microgel [21] and finally a more complex *0.45 wt.%* aqueous κ-Carrageenan gel that is thixotropic and very prone to syneresis. The syneresis phenomenon is the contraction of a gel that occurs accompanied by the separation or segregation of the dispersing fluid. In this case, the attractions between the helix-shaped molecules of κ-Carrageenan reduce the free volume of the gel and expel part of the aqueous phase over time, leading to phase separation [22]. We measure the steady two-dimensional velocity field and assess the validity of the *Couette analogy* as compared to the Owens *et al.* [19] analysis. In addition, by comparing results obtained with the 24-arm fVIC geometry with a cylindrical Couette and a 6-blade cruciform vane geometries, we study the effect that the OAF of the measuring geometry has on disrupting the κ-Carrageenan gel during immersion. Our PIV measurements show that the fractal vane produces rigid body-like motion for almost all the fluid in between the vane arms, as well as axisymmetric flow field in the annular gap out to the bounding wall cup for the Newtonian fluid and the model microgel. In addition, the effective shearing radius of the fractal vane fixture $R_{eq}$ remains constant in each fluid, allowing the use of the *Couette analogy* and the Owens *et al.*

analysis, both with outstanding accuracy. However, even the initial immersion of the measuring geometries into the κ-Carrageenan gel accelerates syneresis that results in shear-banding for both the Couette and fractal vane in cup flows. This disturbance of the sample during rheometrical fixture immersion is attributed to shearing/compression of the sample, which cannot be avoided regardless of specific geometric fixtures. Despite this fact, the present set of results validates the 24-arm fVIC geometry as a reliable rheometrical tool for a variety of complex fluids.

## II. MATERIALS AND METHODS

### II.1 Materials

The fluids utilized in this work were a Newtonian fluid (glycerol from Drogueria Cosmopolita, Mexico), a non-thixotropic yield-stress fluid consisting of an aqueous microgel containing *0.12 wt.%* of poly(acrylic acid) (Carbopol® 940, Lubrizol) and a hydrogel of *0.45 wt.%* of κ-Carrageenan (Drogueria Cosmopolita, Mexico). Hollow glass particles (Potters Industries) of *10 μm* in size and having a specific gravity of *1.1 ± 0.05* were added into the dispersions at concentrations of *0.03 wt.%*, *0.03 wt.%* and *0.05 wt.%* for the glycerol, Carbopol®, and κ-Carrageenan, respectively, to serve as flow tracers.

The glycerol and Carbopol® microgel have been well-characterized previously in cruciform VIC, Couette and parallel-plate geometries and their rheological behaviors are described in detail elsewhere [7, 23-25]. The glycerol was used as received, after dispersing the seeding particles in it by stirring for *1 h*. Regarding the microgel, this was prepared by dispersing the proper amount of Carbopol® 940 in bidistilled water at *500* rpm for *3 h* with a twisted-three blade turbine impeller attached to a speed-controlled agitator. After that time, the PIV tracer particles were added to the dispersion and left under stirring for another

hour. Then, the dispersion was neutralized with a *5 mol/l* NaOH solution to reach a pH value of *7.03 ± 0.03*. The microgel was held under quiescent conditions at ambient temperature for *1* day prior to being used in the fVIC flow.

As for the κ-Carrageenan gel, this was obtained by dispersing the proper amount of polymer in bidistilled water under constant stirring using a high-efficiency magnetic stirrer (Spinstar®). Then, the temperature was gradually increased until reaching *60 °C*, value that was kept for *10 min*. Afterwards heating was stopped and the tracer particles were aggregated to the solution under continuous stirring while the temperature was lowered to *26 °C*. Once the temperature reached *26 °C*, stirring was stopped and the solution was left to stand for 19 hours at room temperature. This procedure results in thermoreversible gels with syneresis and without added salts [26]. A basic rheometrical characterization of the κ-Carrageenan gel (dynamic oscillatory and continuous shear) is provided in appendix A.

Finally, for rheometrical measurements (see below), the gel samples were gently loaded into the cup up to a previously preset volume by using a plastic spoon with minimal shaking, so as not to induce much distortion in their bulk. Then, the as filled cup was allowed to rest for three minutes before immersing the measurement geometry at a rate of 300 μm/s. This procedure resulted in reproducible initial testing conditions for both, the Carbopol® and κ-Carrageenan gels and different fixtures.

## II.2 Measurement geometries

### II.2.1 The 3D-printed fractal vane

The bespoke 3D-printed fractal vane utilized in this work was coupled to a rotational controlled-stress rheometer (UDS 200 Paar Physica). This vane was designed according to the characteristics reported by Owens *et al.* [19] using a three-generation finite

Bethe network with 24 contact points at $R_V$ or 24-arm vane. Its peripheral dimensions correspond with those of a standard concentric cylinder geometry of radius $R=14\ mm$ and length $L=42\ mm$, which makes it suitable to characterize different complex fluids by simply changing the gap between the pair (vane tips and cup) or modifying the surface characteristics of the cup. The fractal vane was attached to the stainless-steel coupling of the UDS 200 rheometer by means of a pin and a stud bolt (see Fig. 1).
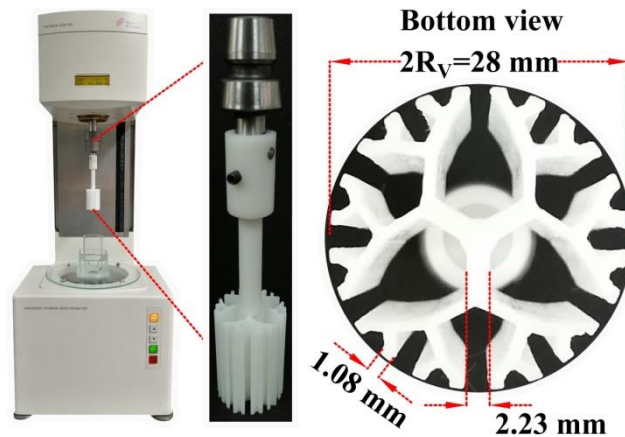


Figure 1. The 3D printed fractal vane and its coupling to the UDS 200 rheometer.

The fractal vane was manufactured by 3D printing using a laser stereolithography (SLA) printer (XFAB 2500SD, DWS Systems) and the Rigid 4000 resin from FormaLabs (GEMBA Engineering S.A. de C.V.). According to its material datasheet, this resin has Young's and flexural moduli of *2.1 GPa* and *1.4 GPa* without additional curing, respectively, and maximum tensile and flexural strengths of *33 MPa* and *43 MPa* without additional curing, respectively. The vane was printed vertically, starting with the vane body and ending at the rheometer coupling shaft to ensure its concentricity. One-piece printing took approximately *3 h* with a layer thickness of *100 μm*. Finally, the printed vane was used in green, that is, without additional UV curing.

The 3D-printed fractal vane was coupled to the rheometer as described above. As for the cup, this was constructed out of Duran® borosilicate glass (Schott) with *80 mm* in height. The inner surface of the cup was clean and its radius, *R*, was *18.65 mm*, rendering a gap of *4.65 mm*. Thus, the distance from the bottom of the vane to the bottom of the cup was *4 mm*, and the cup was filled with fluid up to a height of *50 mm*.

### II.2.2 The Couette and the 6-blade vane geometries

A Couette and a 6-blade vane geometries were utilized to further analyze the flow behavior of the κ-Carrageenan gel using rheo-PIV. The Couette cell consisted of an inner cylinder (bob) made up of black-painted aluminum with *41.4 mm* in height and radius $R_i=13.8$ *mm,* and a cup made up of clean borosilicate glass with radius *R=15 mm* *(k=$R_i$/R=0.92)* [24]. On the other hand, the VIC system consisted of a 6-blade cruciform stainless steel vane with $R_V=11$ *mm* [7], in conjunction with the cup mentioned above.

### II.3 Rheo-PIV set-up

The experimental set-up utilized in this work is shown in Fig. 2 with the fVIC geometry and an amplification of the region of interest (ROI). It is the same set-up used by Medina-Bañuelos *et al.* for the analysis of the steady tangential annular (Couette) [23, 24] and VIC flow [7] of the same glycerol and Carbopol® microgel. Then, only a brief description is provided here.
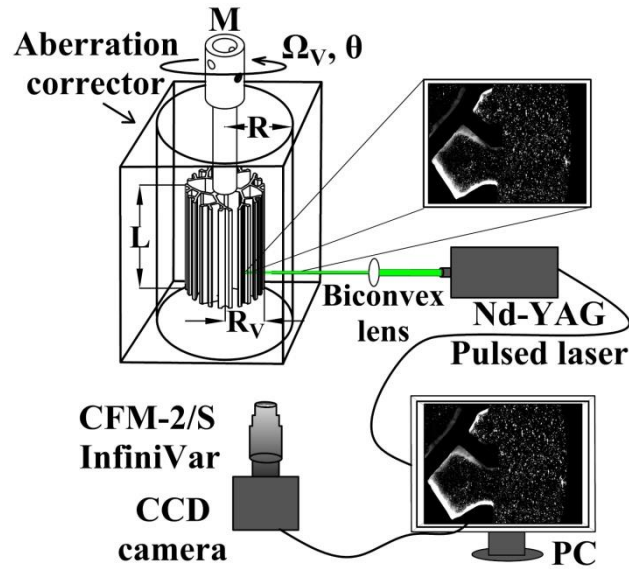
Figure 2. Experimental set-up for the rheo-PIV measurements with the 24-arm fVIC geometry.

A 2D PIV system (Dantec Dynamics) consisting of a high-speed and high-sensitivity CCD camera (HiSense MKII), two coupled Nd:YAG lasers (SoloPIV II, New Wave Research), *50 mJ* and *λ = 532 nm*, and Dantec Dynamic Studio 2015a software for image acquisition and analysis was utilized for the PIV measurements. To increase the spatial resolution, a variable focal length microscope (InfiniVar CFM-2/S, Infinity) was attached to the CCD camera. As previously reported [7], the PIV data were collected in the $r\theta$ plane at a fixed height, which due to the different sizes of the geometries used resulted in different measurement position for each fixture, namely, *7.5 mm* from the fractal vane bottom, at *8 mm* from the 6-blade VIC bottom and at *5 mm* from the Couette bob bottom, respectively. Measurements at such heights allow for minimization of the influence of end effects. The ROIs for determining the velocity distributions covered a slice between two adjacent arms of the fVIC geometry, a slice between two adjacent blades of the 6-blade

11

vane and a slice of *10°* in the Couette cell, respectively, including the whole gap. Velocity maps in the ROI were obtained at different torque, *M*, values, while measuring the corresponding angular speeds of the vane, $\Omega_V$. Fifty pairs of images were acquired for each flow condition and correlated independently to obtain the corresponding velocity maps, which were then averaged in time to obtain a single velocity map (see Fig. 3) for steady flow conditions. The velocity distributions reported here, $V_\theta$, were selected from the ROI at $\theta = 0°$, where the radial component of the velocity, $V_r$, was ~0 (see blue dotted vertical line in Fig. 3). All the data reported in this work were obtained under torque-controlled conditions and those for the Newtonian fluid and the microgel are steady-state ones. For this, the torque was gradually increased until the target value was reached. Finally, all the experiments were run with preheated samples at a temperature of *T=25±1°C* in a laboratory with controlled climate.
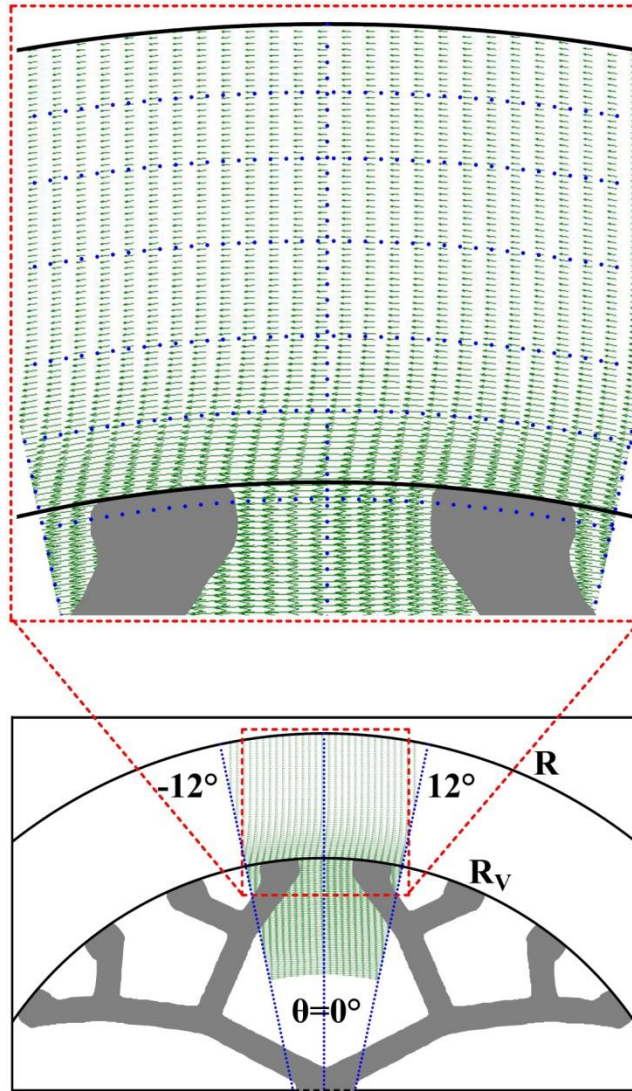
Figure 3. ROI for PIV measurements and zoom of the velocity map in the 24-arm fVIC flow.

## III. RESULTS AND DISCUSSION

### III.1 Rheo-PIV of the fractal vane-in-cup flow of the Newtonian fluid

The velocity distributions of glycerol in the fVIC geometry are shown in Figs. 4a-b along with those predicted by the *Couette analogy* for different imposed torque values. For this, the tangential velocity, $V_\theta(r)$, is expressed in terms of $R_{eq}$ as [7, 15]:

$$V_\theta(r) = \Omega_V \frac{R_{eq}^2}{r} \frac{R^2 - r^2}{R^2 - R_{eq}^2} \quad (1)$$

Where $r$ is the radial position and $\Omega_V$ is the angular speed of the fractal vane. It can be seen from Figs. 4a-b that the velocity increases linearly with the radial distance up to $R_{max}$ (~13.66 mm), which remains constant and is very close to $R_V$ for all the imposed torques (see Fig. 5a). In other words, the velocity distributions describe a rigid body-like motion (absence of secondary flow) with constant angular speed, $\Omega(r) = V_\theta(r)/r$, up to $R_{max}$. The dashed lines, whose slopes represent the $\Omega_V$ values, intercept the calculated velocity profiles at $R_{eq} = 13.87$ mm, this value, akin to $R_{max}$, does not change with the imposed torque. This is better illustrated in Fig. 4c, in which the set of velocity distributions in Figs. 4a-b have been normalized, as well as in Fig. 5b, where the ratio $R_{eq}/R_V$ has been plotted as a function of the ratio $M/M_{max}$, with $M_{max}$ the highest imposed torque for each fluid. From $R_{eq}$, the velocity distributions describe a shear flow and extrapolate to zero velocity at the wall, as expected for a Newtonian behavior. Also, the measured velocity profiles and those obtained using the *Couette analogy*, Eq. (1), are in very good agreement up to $R_{eq}$ within 2%. Meaning of the different radii and ratios ($R_{eq}$, $R_{max}$, $R_{eq}/R_V$) and their values for the fluids studied in this work are summarized in Tables 1 and 2, respectively. The deviation of the PIV data from $\Omega = constant$ and Eq. (1) for $R_{max} < r < R_V$, i. e., around the maxima in the velocity profiles, and the existence of such maxima are consistent with previous reports [7, 15] for the 6-blade VIC flow of Newtonian and non-Newtonian fluids. This deviation has been attributed to extensional flow in such a region.
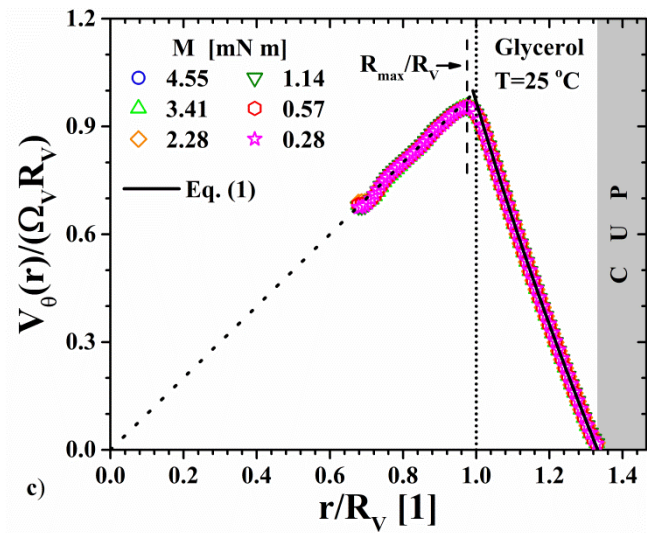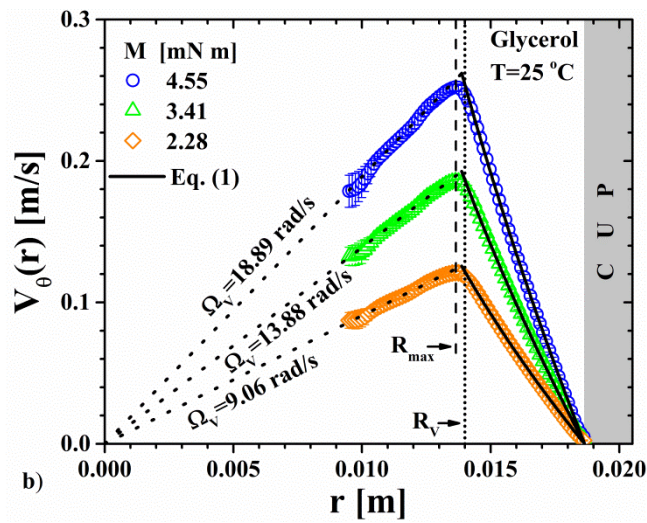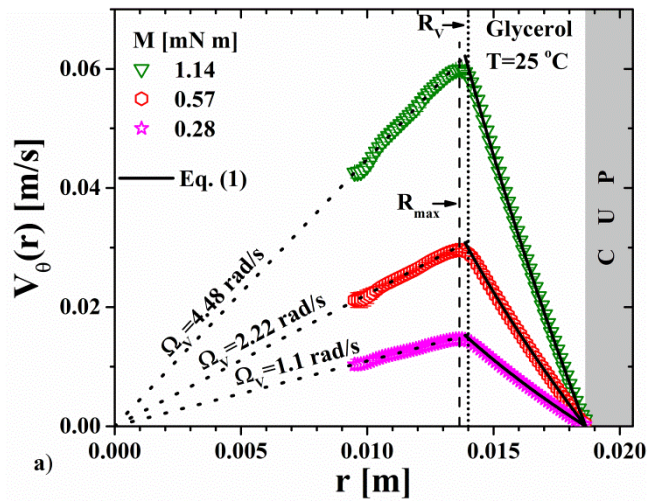
Figure 4. Velocity distributions, $V_\theta(r)$, in the 24-arm fVIC geometry for the Newtonian fluid, glycerol, determined with the PIV method for six vane rotational speeds. (a) $\Omega_V =$ *1.1, 2.22* and *4.48 rad/s* and (b) $\Omega_V$ = *9.06, 13.88* and *18.89 rad/s.* c) Normalized velocity distributions for different torque values. Dotted lines indicate the different vane rotational speeds. Continuous lines indicate the theoretical velocity profiles, i.e., Eq. (1), for $R_{eq}=$ *13.87 mm*.
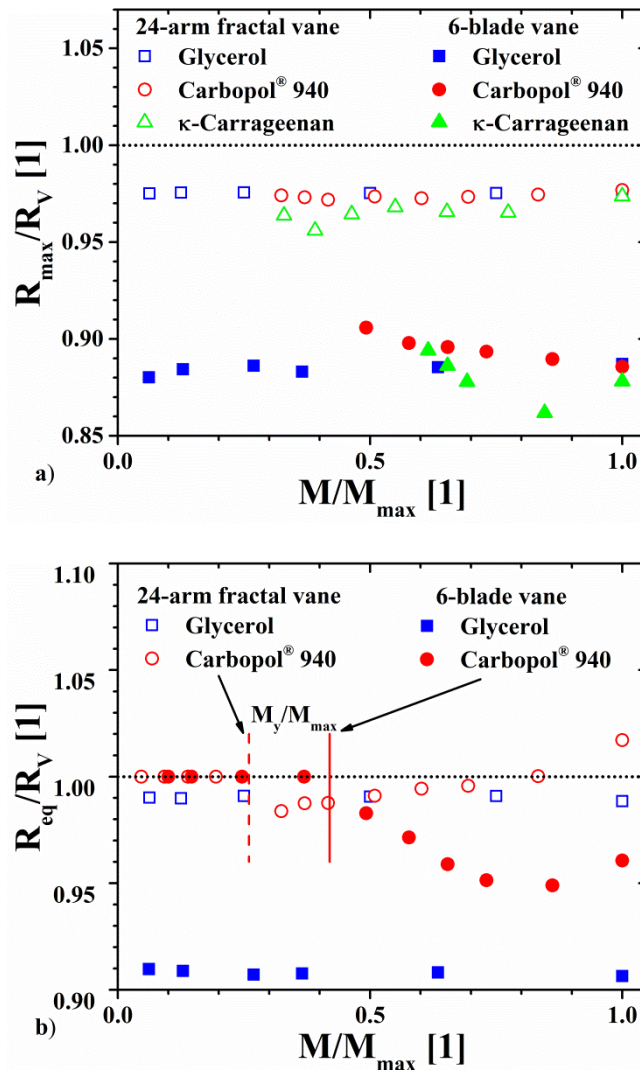


Figure 5. a) $R_{max}/R_V$ versus $M/M_{max}$ for glycerol, and Carbopol® and κ-Carrageenan gels in the 24-arm fVIC geometry, as well as for glycerol and Carbopol® microgel in the 6-blade VIC geometry. b) $R_{eq}/R_V$ versus $M/M_{max}$ for glycerol and Carbopol® microgel in the 24-arm

fVIC geometry, as well as for glycerol and Carbopol® microgel in the 6-blade VIC geometry. The dashed and continuous vertical red lines indicate the ratio of torque at yielding, $M_y$, and the maximum imposed torque, $M_{max}$, $M_y/ M_{max}$, for the Carbopol® microgel in the 24-arm fVIC and 6-blade VIC, respectively. Data for glycerol and Carbopol® microgel in the 6-blade VIC flow are reproduced from [7].

Table 1. Definition of radii for the vane tools and *Couette analogy*.

| Name | Symbol |
|---|---|
| Vane radius | $R_V$ |
| Equivalent radius. Radius of shearing of the "imaginary" fluid cylinder formed between arms of a vane tool that would exert the same stress as an equivalent bob. | $R_{eq}$ |
| Radial location of maximum velocity in VIC flows. | $R_{max}$ |

Table 2. $R_{eq}$, $R_{max}$ and $R_{eq}/R_V$ in the 24-arm fVIC and 6-blade VIC flows for different fluids. Data for 6-blade VIC are from [7].

| Fluid | 24-arm fVIC | | | 6-blade VIC | | |
|---|---|---|---|---|---|---|
| | $R_{eq}$ [mm] | $R_{max}$ [mm] | $R_{eq}/R_V$ | $R_{eq}$ [mm] | $R_{max}$ [mm] | $R_{eq}/R_V$ |
| Gycerol | 13.87±0.02 | 13.66±0.02 | 0.99 | 9.99±0.01 | 9.71±0.04 | 0.91 |
| Carbopol microgel | 13.87±0.08 | 13.63±0.02 | 0.99 | 10.81-10.44 | 9.96-9.79 | --- |
| $\kappa$-Carrageenan | --- | 13.51±0.07 | --- | --- | 9.84-9.48 | --- |

Another interesting observation from Figs. 4c and 5a is the fact that $R_{max}$ is much closer to $R_V$ for the 24-arm fVIC ($R_{max}/R_V= 0.975$) than in the 6-blade VIC flow of glycerol ($R_{max}/R_V=0.883$ from [7]), which indicates that the flow field is axisymmetric in a larger region in the fVIC than in the 6-blade VIC geometry. We have applied the *Couette analogy*

using the rheometrical and PIV data, respectively, to construct the flow curve of the fluid, for this, the shear rate, $\dot{\gamma}_{r\theta}(r)$, is given by:

$$\dot{\gamma}_{r\theta}(R_{eq}) = \frac{2\Omega_V}{d\log M / d\log \Omega_V} \quad (2)$$

For a Newtonian fluid, Eq. (2) becomes:

$$\dot{\gamma}_{r\theta}(R_{eq}) = \frac{2\Omega_V}{1-\left(R_{eq}/R\right)^2} \quad (3)$$

and the shear stress, $\sigma_{r\theta}(r)$, is calculated as [25]:

$$\sigma_{r\theta}(r) = \frac{M}{2\pi L r^2 C_L} \quad (4)$$

Where $L$ is the length of the inner cylinder and $C_L=1.23$ is a calibrated correction factor for end effects [24], which was calculated from comparison with cone and plate data for this fluid. This stress distribution is valid independently of the type of fluid and boundary conditions. Meanwhile, the shear rates for the PIV data were calculated from the local derivative of the velocity distributions as $\dot{\gamma}_{r\theta}(r) = -r\,d(V_\theta/r)/dr = -r\,d\Omega/dr$. The resulting flow curves are shown in Fig. 6, along with those obtained by using a cone and plate rheometer and the Owens *et al.* [19] analysis, in which the shear rate is computed by simply replacing $R_{eq}$ by $R_V$ in Eq. (3), whereas the wall shear stress is calculated using the torque-stress conversion formula for a N-arm vane [19]:

$$\sigma_w = \frac{M}{2\pi R_V^2 L\left[\left(1-\frac{1.113}{N}\right)+\frac{R_V}{4L}\left(2.75-\frac{3}{\sqrt{N}}\right)\right]} \quad (5)$$

In Eq. 5, the sensitivity of the flow to the number of outer contact points and end effects of the finite-length vane is accounted for by the terms between square brackets. Note in

addition that Eq. (5) does not require *a priori* knowledge of a $R_{eq}$ value. Thus, as seen from Fig. 6 the superposition of the different flow curves is remarkable, which validates our experimental protocol, as well as substantiates the use of the *Couette analogy* and the torque-stress conversion formula [Eq. (5)] for the Newtonian fluid in the fVIC geometry. In particular, according to Owens *et al.* [19], Eq. (5) allows for computation of the wall shear stress from a more axisymmetric flow field as the number of arms increases, which agrees with the symmetry of the flow field in a larger region in the fractal vane than in the 6-blade vane as discussed above. Therefore, considering this result, it is also expected that both $R_{max}$ and $R_{eq}$ tend to $R_V$ with increasing the number of blades or arms in a vane fixture.

To close this section and for the purpose of completeness, in Fig. 6 we have included the flow and viscosity curves calculated using the $R_V$ value of the fractal vane in Eqs. 3 and 4, i. e., using the *Couette analogy* without *a priory* known $R_{eq}$. In that case, the error introduced by using $R_V$ instead of the appropriate $R_{eq}$ amounts ~*2.0%* in the viscosity computation, which is a very good approximation for practical purposes.
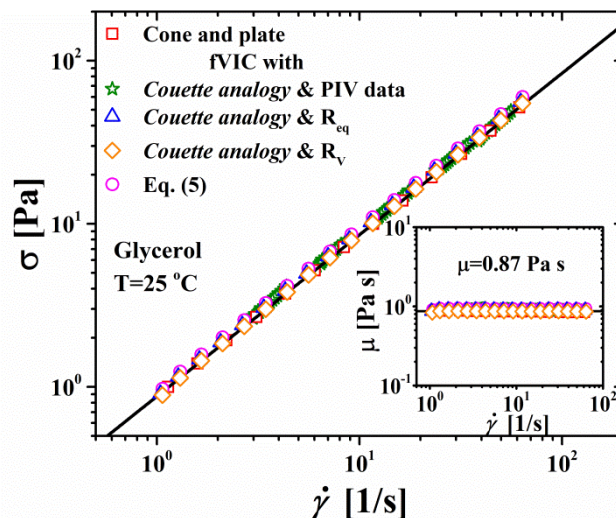


Figure 6. Flow and viscosity curves for glycerol using different methods.

*III.2 Rheo-PIV of the fractal vane-in-cup flow of the Carbopol® microgel*

The steady torque *versus* vane rotational speed data for the Carbopol® microgel obtained with the fVIC geometry are shown in Fig. 7. A transition in behavior appears to be occurring between the fourth and fifth applied torques, which signals the yielding of the microgel. Thereafter, the rotational speeds of the vane increase significantly with the imposed torques, evidencing the onset of flow and shear-thinning of the microgel.
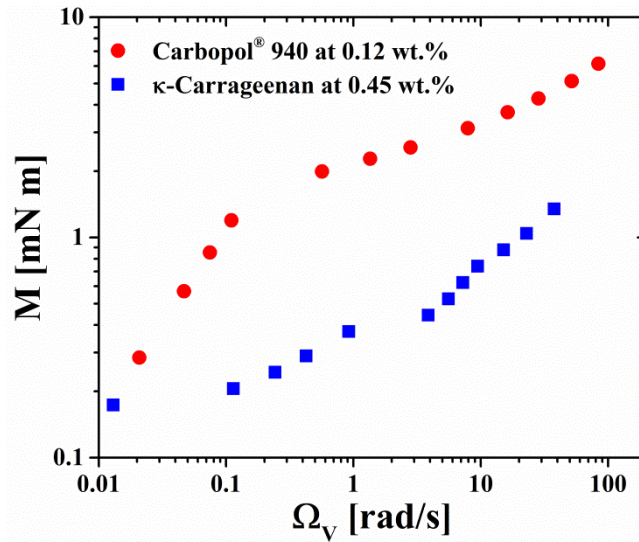


Figure 7. Torque *versus* rotational speed curves for the Carbopol® and κ-Carrageenan gels in the 24-arm fVIC flow. Carbopol® microgel data are steady, while those of the κ-Carrageenan gel data were collected *100 s* after torque imposition.

The distributions of the magnitude of the velocity vector for the microgel in a slice (*-12°≤θ≤12°*) for the lowest (*2.28 mN m*) and highest (*5.12 mN m*) steady torque values with shear flow are shown in Figs. 8a-b, respectively. The velocity of the fluid remains constant with respect to $\theta$ for a given $r$ in the gap; see for example, the fine yellow circular line close to $R_V$ in Figs. 8a-b, which indicates that both the velocity and shear stress fields are spatially axisymmetric up to very close to $R_V$, with cylindrical shear surfaces even at

high rotational speeds. This strongly contrasts with the observation by Medina-Bañuelos *et al.* [7] for the same microgel in a 6-blade cruciform VIC (see Figs. 6a-b in [7]), in which the tangential velocity was dependent upon the $\theta$ direction near the blades even at much lower rotational speeds than in the fVIC, resulting in the already reported polygonal shape in the neighborhood of the blades [10-17]. Also, note that the velocity distributions seem to be continuous across the gap and that there is slip at the wall cup $(V_\theta(R)\neq0)$.
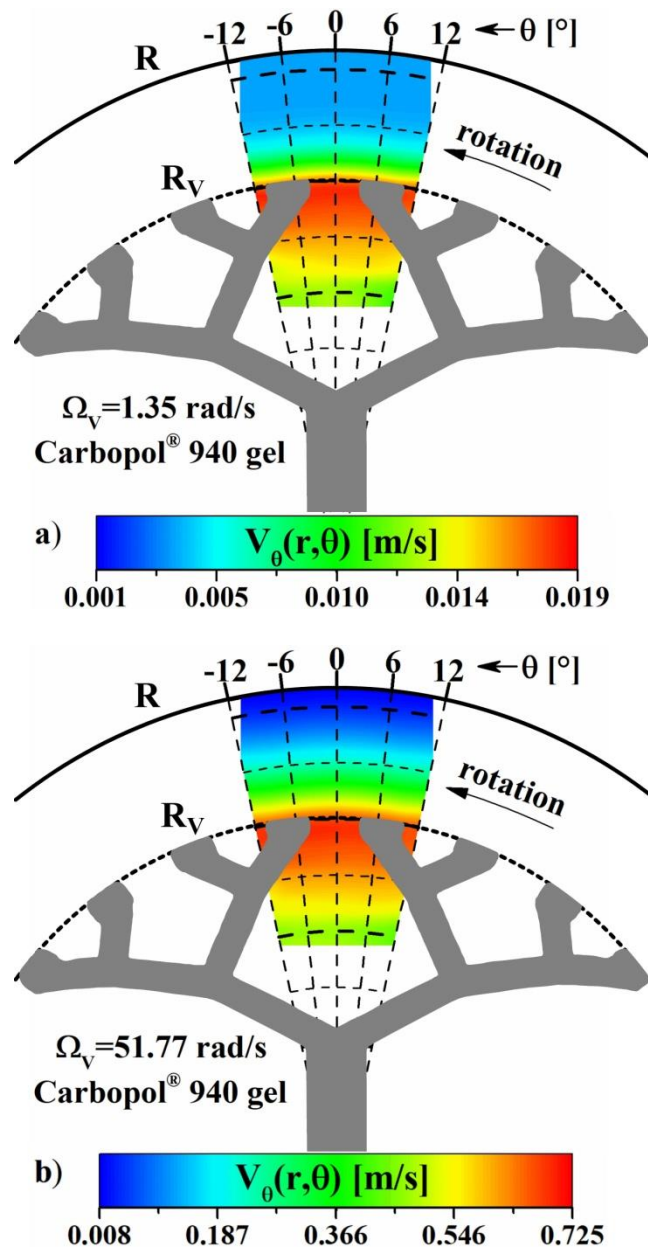
Figure 8. Magnitude of velocity distributions under steady state for the Carbopol® microgel in the 24-arm fVIC geometry. (a) $\Omega_V = 1.35\ rad/s$ and (b) $\Omega_V = 51.77\ rad/s$. Two arms located at $\theta = -12°\ and\ 12°$.

The velocity distributions $V_\theta(r)$ of the microgel in the fVIC flow determined using PIV at $\theta = 0°$ are shown in Figs. 9a-c for twelve torque values. For the first four torques (Fig. 9a), the velocity increases linearly with radial distance in the whole flow region, indicating that the shear stress at all radial locations is smaller than the yield stress, $\sigma_y$, of the fluid, so that the entire microgel sample undergoes rigid body-like motion or plug flow. Also, the velocity profiles show non-zero values at the outer cylinder, evidencing slip at the wall cup, with a slip velocity $U_S(\sigma_w(R))$ that originates the plug flow. The slip behavior of this microgel in the Couette and VIC flows has been studied in detail previously [7, 23, 24] and shall not be further discussed here. In the end, it can be seen that the $\Omega$ values of the fluid determined from the velocity distributions reported in Fig. 9a (hollow symbols) match very well with those $\Omega_V$ measured by the rheometer (dashed lines); we have calculated a maximum difference of 2.5, 0.9, 0.9 and 3.0% with respect to the expected values for $\Omega_V=$ 0.021, 0.047, 0.075 and 0.11 rad/s, respectively, which further validates our PIV measurements.
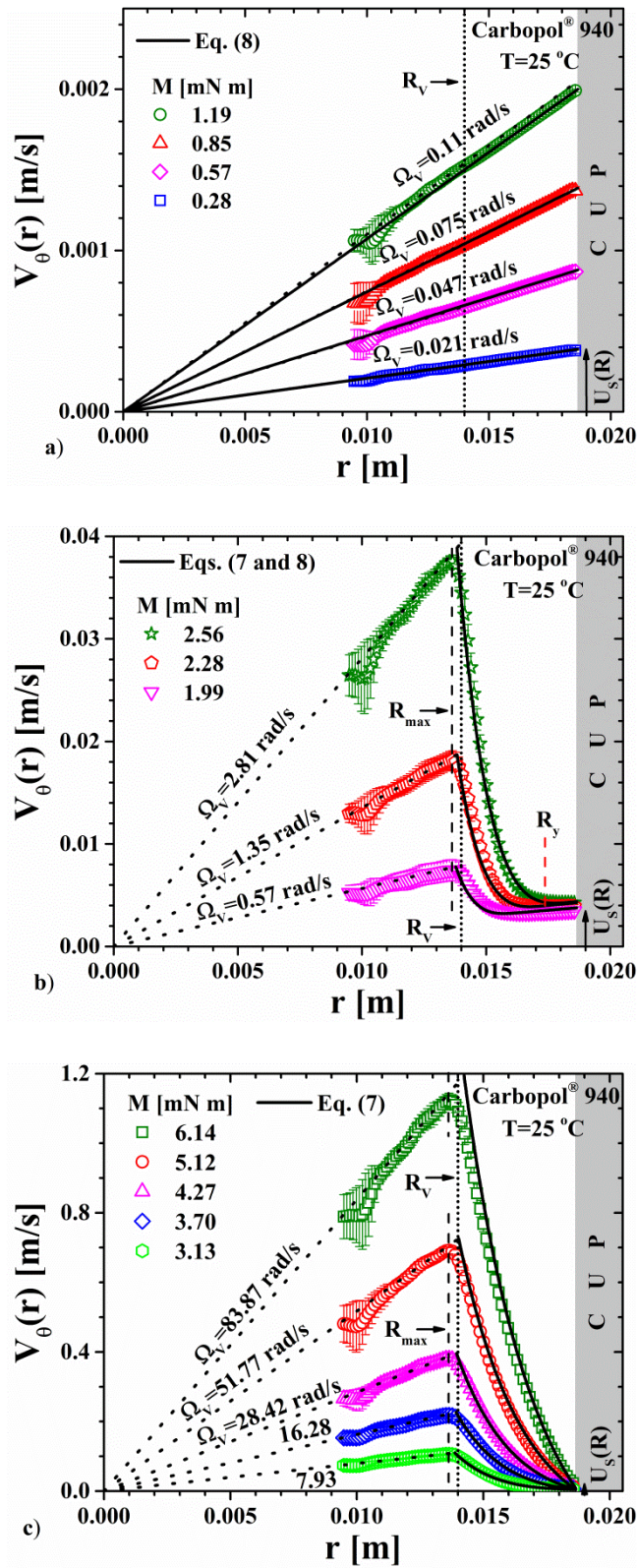
Figure 9. Velocity distributions $V_\theta(r)$, for the Carbopol® microgel in the 24-arm fVIC geometry at various vane rotational speeds at $\theta = 0°$. *a) $\Omega_V=$ 0.021, 0.047, 0.075* and *0.11*

*rad/s; b)* $\Omega_V$= *0.57, 1.35* and *2.81 rad/s; c)* $\Omega_V$= *7.93, 16.28, 51.77* and *83.87 rad/s.* Dotted lines indicate the different vane rotational speeds. Continuous lines indicate the theoretical profiles calculated with Eqs. (7) and (8).

Increasing the torque above *1.19 mN m* (Figs. 9b) results in the appearance of three well-defined zones in the velocity distribution: one internal to the vane for $r<R_{max}$ with rigid solid-like motion, one in the gap between the vane and cup with shear flow, and one near to the wall cup in which the fluid again rotates as a solid body, with slip at the wall cup. The first two regions are separated by a narrow gap between $R_{max}$ ($R_{max}<R_V$) and the position for the onset of flow. The shape of these profiles is a sign that $\sigma_y$ has been surpassed from $R_V$ up to the radial position of the outer yield surface, $R_y$ (see Figure 10 below, as well as [7, 18, 23]), beyond which the fluid again moves as a solid body (Fig. 9b). At even higher imposed torques (Fig. 9c), above *3.13 mN m,* $\sigma_y$ is exceeded in the whole gap, and the fluid is subjected only to shear flow with slip at the wall cup. The slip velocity for this microgel is a function of the imposed torque (shear stress) and its trend in the different flow regimes has been reported elsewhere [7, 23]. Note in addition that the fluid trapped inside the vane keeps moving as a solid in rotation up to a position $R_{max}$ that lies very close to $R_V$, as previously described for the Newtonian fluid. This result indicates that, indeed, the fractal vane with the fluid in between can be considered as a solid cylinder that shear the rest of the sample in the gap without apparent slip effects at the rotating "interface" at $R_V$. It is noteworthy that the position of the maxima in the velocity distributions $R_{max}$ does not change significantly with the imposed torque (see Fig 5a). Moreover, the ratio $R_{max}/R_V$ reaches the same value for the Newtonian fluid and the microgel independently of the imposed torque (see Fig. 5a). This is an interesting result that

contrasts with the observed behavior of the same microgel in [7], in which $R_{max}$ changed with the type of fluid and with the flow conditions for the microgel, leading to the indeterminacy of the $R_{eq}$ value to apply the *Couette analogy* for non-Newtonian fluids. Then, since the overall characteristics of the fVIC flow of the microgel resemble those reported by Medina-Bañuelos *et al.* for the same fluid in Couette flow [23] and since $R_{max}$ does not change with flow conditions, the use of the *Couette analogy* with slip at the cup is viable to describe the microgel flow behavior, such a description is provided below.

Three types of flows are possible for viscoplastic fluids in a Couette geometry with a rotating bob and slip at the fixed cup (see Fig. 10): (I) rigid body-like motion or pure plug flow over the entire gap when $\sigma_{r\theta}(kR) < \sigma_y$ (see Fig. 9a); (II) shear deformation and plug flow that are simultaneously occurring at different regions if $\sigma_{r\theta}(kR) > \sigma_y > \sigma_{r\theta}(R)$; in this case, the plug flow would occur adjacent to the outer cylinder (see Fig. 9b); and (III) shear deformation of the fluid over the entire gap if $\sigma_{r\theta}(R) > \sigma_y$ (see Fig. 9c). For viscoplastic fluids in torsional flows with wall slip, the slip velocity $U_S$ is defined as the difference between the velocity of the fluid adjacent to the wall and the velocity of the wall. The slip velocity is given as $U_S = \pm\beta\sigma_w^{s_b}$, where $\sigma_w$ is the shear stress at the wall, $\beta$ is the slip coefficient and $s_b$ is the slip exponent; both are dependent on the fluid, the materials of construction, and the surface characteristics of the flow channel [28, 29]. Also, $\beta$, and $s_b$ can be functions of the flow conditions for microgels [30-32]. There can be two wall slip velocities in Couette flow, i.e., $U_S(kR)=V_\theta(kR) - \Omega_i kR$ and $U_S(R)=V_\theta(R)$ at the inner and outer walls of the annulus, respectively, where $V_\theta(kR)$ and $V_\theta(R)$ are the tangential velocities of the fluid at the bob and wall cup, respectively, and $\Omega_i$ is the independent angular speed of the bob. Then, $U_S(kR) < 0$ and $U_S(R) > 0$. In the treatment of the VIC

flow, we assume, based on observations, that there is no slip at the surface of the fluid constituting the rigid body, i.e., at $R_{eq}= kR$ [3]. The assumption of $U_S(kR)=U_S(R_{eq}) = 0$ is based on the fact that the bob, considered to consist of the fluid in rigid body-like motion (ignoring the vane arms), is transferring its $\theta$-*momentum* to the fluid in the gap, i.e., for $R_{eq} \leq r \leq R$. Thus, with this assumption, there would be a no-slip condition at $R_{eq}= kR$ and wall slip can occur only at $r = R$.
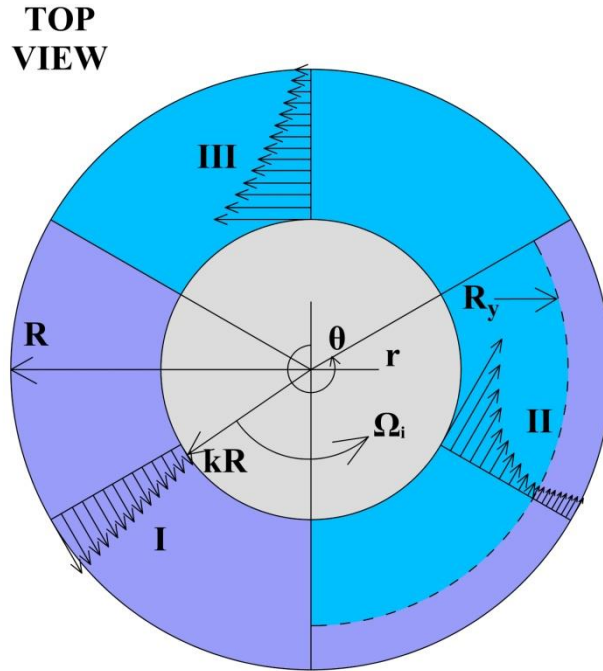


Figure 10. Schematic representation of the annular flow region in a Couette cell showing the three possible flow regimes in the presence of slip at wall cup, namely, (I) pure plug flow in the entire gap for $\sigma_{r\theta}(kR) < \sigma_y$, (II) shear flow for $kR \leq r < R_y$ $(\sigma_{r\theta}(kR) \geq \sigma_{r\theta}(r) \geq \sigma_y)$ and plug flow for $R_y \leq r \leq R$ $(\sigma_y > \sigma_{r\theta}(r) \geq \sigma_{r\theta}(R))$, finally, pure shear flow for $\sigma_{r\theta}(R) > \sigma_y$ (III).

Let us consider a Herschel-Bulkley fluid for which we can define the stress and velocity relationships in cylindrical coordinates:

$$\sigma_{r\theta} = \sigma_y + K\left(-r\frac{d}{dr}\left(\frac{V_\theta}{r}\right)\right)^{n-1}\left(-r\frac{d}{dr}\left(\frac{V_\theta}{r}\right)\right) \qquad for \ \sigma_{r\theta} > \sigma_y \qquad (6a)$$

$$-r\frac{d}{dr}\left(\frac{V_\theta}{r}\right) = 0 \qquad for \ \sigma_{r\theta} \leq \sigma_y \qquad (6b)$$

The yield stress, $\sigma_y$, the consistency index, $K$, and the shear rate sensitivity index (power-law index), $n$, are the three characteristic parameters. Viscoplasticity requires that the shear rate is zero when $\sigma_{r\theta} < \sigma_y$. The shear stress profile for steady, isothermal, and creeping tangential annular flow of incompressible fluids can be obtained from the momentum equation in the $\theta$-direction. In this case, the velocity distributions for the deformation, $V_\theta^{III}(r)$, and the plug flow, $V_\theta^{I}(r)$, zones are determined starting with $\sigma_{r\theta}(r) = C/r^2 = -\eta(r)r(d(V_\theta/r)/dr)$ (where $\eta(r)$ is the distribution of the true shear viscosity of the fluid) and integration from the inner cylinder, $r=\kappa R=R_{eq}$, to any radial location, $r$. The velocity distribution for the shear flow zone ($\kappa R \leq r \leq R_y$), $V_\theta^{III}(r)$, is given by [7]:

$$\frac{V_\theta^{III}(r)}{r} = \Omega_i - \frac{1}{K^{1/n}}\int_{kR}^{r}\left(\frac{C}{r^2}-\sigma_y\right)^{1/n}\frac{dr}{r} \quad ; \quad for \ \ kR < r < R_y \qquad (7)$$

And for the plug flow zone, $V_\theta^{I}(r)$:

$$\frac{V_\theta^{I}(r)}{r} = \Omega_i - \frac{1}{K^{1/n}}\int_{kR}^{R_y}\left(\frac{C}{r^2}-\sigma_y\right)^{1/n}\frac{dr}{r} = \frac{U_S(R)}{R} \quad ; \quad for \ \ R_y \leq r \leq R \qquad (8)$$

Where $R_y = (C/\sigma_y)^{1/2}$, i.e., $\sigma_{r\theta}(R_y) = \sigma_y$, and $\Omega_i = \Omega_V$ is the angular velocity of the bob or vane. As mentioned before, the constant $C$ is determined from the steady-state torque versus cylinder angular velocity data, $M(\Omega_i)$, where $M = 2\pi L r^2 \sigma_{r\theta}(r) = 2\pi L C$. Eq. (7) alone applies if $\sigma_{r\theta}(R) > \sigma_y$ (pure shear flow) and both Eqs. (7 and 8) would apply if $\sigma_{r\theta}(kR) > \sigma_y > \sigma_{r\theta}(R)$ (coexistence of sheared and plug flow zones).

The velocity distributions predicted by Eqs. (7) and (8) are included in Figs. 9a-c for comparison. Since the $R_{eq}$ value is not known *a priori* for the microgel, it was calculated from the best fit to the velocity profiles using $R_{eq}=13.5\ mm$ as guessing to start iterations. The $R_{eq}$ that minimizes the error between experimental and theoretical velocity profiles (see Fig. 5b) was used in Eqs. (7) and (8). It can be observed that the calculated velocity distributions agree well with those obtained by PIV under both the rigid body-like motion at torques or stresses below the yield one (Fig. 9a) and rigid body-like motion with shear flow or pure shear flow at torques above the yield one (Fig. 9b-c), which indicates that the *Couette analogy* along with the approach by Medina-Bañuelos *et al.* [7] to describe the Couette flow of Herschel-Bulkley fluids with slip at the walls may be safely used to analyze the fVIC flow of the microgel with slip at the cup.

On the other hand, the ratio $R_{eq}/R_V$ *versus* $M/M_{max}$ values for the microgel are plotted in Fig. 5b along with those calculated for the Newtonian fluid. Note that $R_{eq}/R_V$ is almost the same for the microgel and the Newtonian fluid, is practically constant in the whole range of torques and is very close to $R_V$ ($R_{eq}/R_V=0.993\sim1$), except for those values $M\sim M_y$, where a slight decrease in $R_{eq}/R_V$ occurs right after yielding. However, it is noteworthy that $R_{eq}/R_V$ may well be obtained from pure shear flow data, i. e., from data obtained when the whole volume in the gap is undergoing shear flow. Once again, this result contrasts with the equivalent for the microgel in the 6-blade VIC system, where $R_{eq}/R_V$ decreased under shear flow conditions preventing the application of the *Couette analogy*. The decrease in $R_{eq}/R_V$ right after yielding in both vanes is attributed to experimental uncertainty in the fractal vane and to shear thinning or inertial effects in the 6-blade vane as explained next. First, note that the $R_{eq}$ values are obtained from fitting of the theoretical velocity distributions in Eqs. (7) and (8). For torques (stresses) just above $M_y$

($\tau_y$) the fitting for the fractal vane is not so good because most of the fluid in the gap has not yielded. At even higher torques (stresses) most of the fluid in the gap is already undergoing shear flow, then the fitting is better and $R_{eq}/R_V \sim 1$, as expected for a cylindrical bob (see Figs 9a-c). Also, note that deviation from $R_{eq}/R_V=1$ is around *1%* (see Table 2). In the case of the 6-blade vane we have previously shown [7] that $R_{eq}$ is shear rate sensitive.

Considering the possible practical relevance of the fractal vane, we have calculated the shear stress in the microgel by using Eq. (5) with $R_{max}$, $R_{eq}$ and $R_V$ values, respectively. First, note that the maximum difference between $R_V$ and $R_{max}$ is *6.1%*; meanwhile, between $R_V$ and $R_{eq}$ is *1.6%*, that is, $R_{max}$, $R_{eq}$ and $R_V$ are very close among them for the microgel in the fVIC geometry. Since $R_{max}$ and $R_{eq}$ are not known *a priori*, the use of $R_V$ in Eq. (5) would introduce an error of less than *2%*, which is an excellent approach for practical purposes. Besides, the shear rates calculated by using Eq. (2) (red squares) lie very well on the strip of PIV data (see Fig. 11 below). Moreover, Eq. (2) is expected to work even better with increasing the number of arms of the vane [19]. In its time, however, introducing a larger number of arms may result counterproductive for certain type of fluids, as shown in section *III.4*.

Finally, to test the *Couette analogy* in contrast to the Owens *et al.* analysis [19], we have reconstructed the flow curve of the microgel using the *Couette analogy* with our PIV data as well as using Eqs. (2) and (5) with rheometrical data. For this, the slip contribution to the angular speed was first eliminated by subtracting the slip angular speed at the wall cup, $\Omega_s=Us(R)/R$, from the angular speed measured by the rheometer for each applied torque. Then, the rheometrical data free of slip were fitted to the functional form $M = a+b\Omega^c$ and inserted in Eq. (2) to compute the shear rate. The resulting flow curves

are plotted in Fig. 11 along with that previously obtained for the same microgel using the torsional parallel-plates rheometer with sandpaper [25]. The coincidence among the flow curves is outstanding, which corroborates the validity of both the *Couette analogy* and the Owens *et al*. analysis for the 24-arm fVIC flow of the Carbopol® microgel.
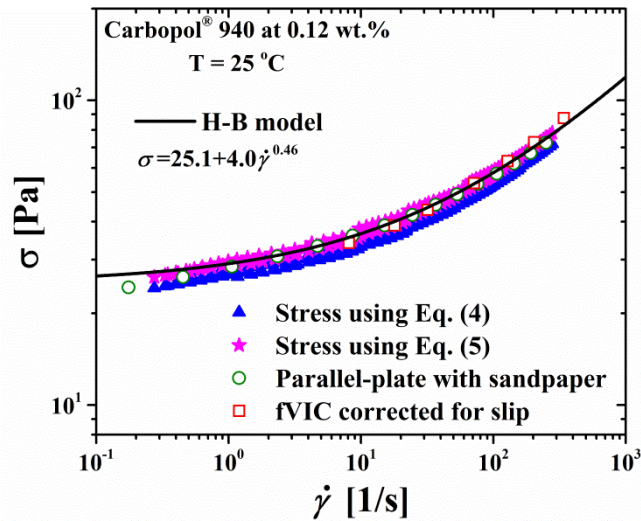


Figure 11. Flow curve of the Carbopol® microgel obtained by different methods. Parallel-plate with sandpaper data are reproduced from [25].

*III.3 Simulation of the fractal vane-in-cup flow of the Carbopol® microgel*

As noted in the introduction, Chaparian *et al*. [18] have recently simulated the vane-in-cup flow of viscoplastic fluids, both with and without wall slip, for conventional cruciform-vanes with various numbers of arms, as well as for fractal vanes with 12 and 24 arms. The authors calculated the spatial distribution of the local kinematics in the mixed flow field induced by rotation of the tool and found that the extensional deformation rate, $\dot{\gamma}_{rr}$, between the arms decreases and that the local homogeneity of the torsional shear rate $\dot{\gamma}_{r\theta}$ improved with increasing the number of arms in the tool. Analysis of the kinematics for a 12-arm fVIC showed that $\dot{\gamma}_{rr} / \dot{\gamma}_{r\theta} < 0.1$, for all Bingham numbers (*Bn*) simulated,

30

resulting in a good rheometric approximation of simple shear flow. Chaparian *et al.* calculated the angular velocity distributions for different vane geometries and compared the computational results for a 6-blade cruciform VIC with slip at the cup against the experimental data reported in [7] for the same geometry; and found excellent agreement between experimental data and simulation.
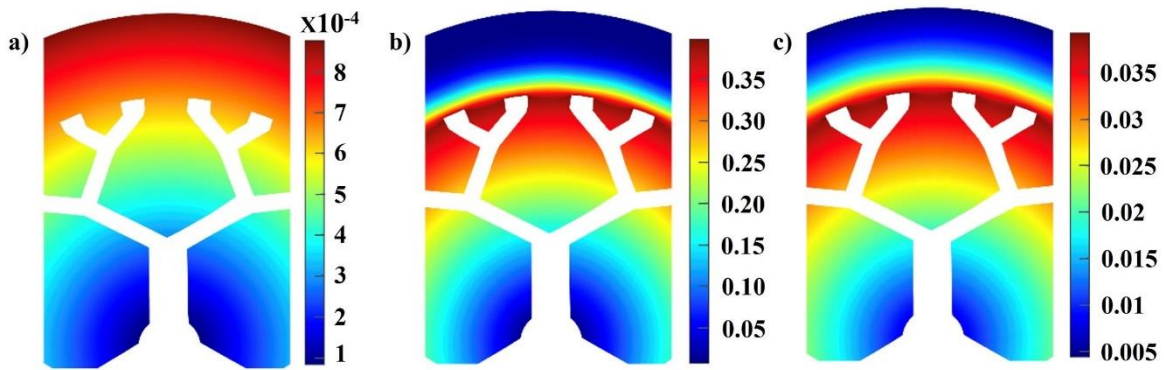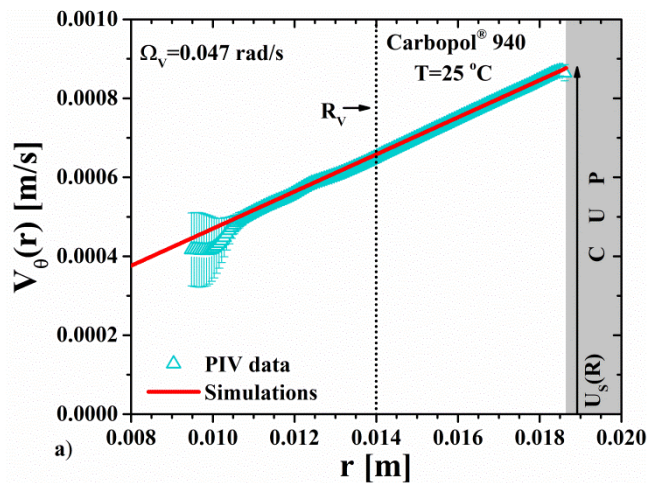


Figure 12. Results from steady numerical simulations with the Hershel-Bulkley model showing the magnitude of the velocity distribution (in [m/s]) for the Carbopol® microgel in the 24-arm fVIC geometry below yielding at (a) $\Omega_V = 0.047$ *rad/s*, and after yielding at (b) $\Omega_V = 2.81$ *rad/s* and (c) $\Omega_V = 28.42$ *rad/s*.
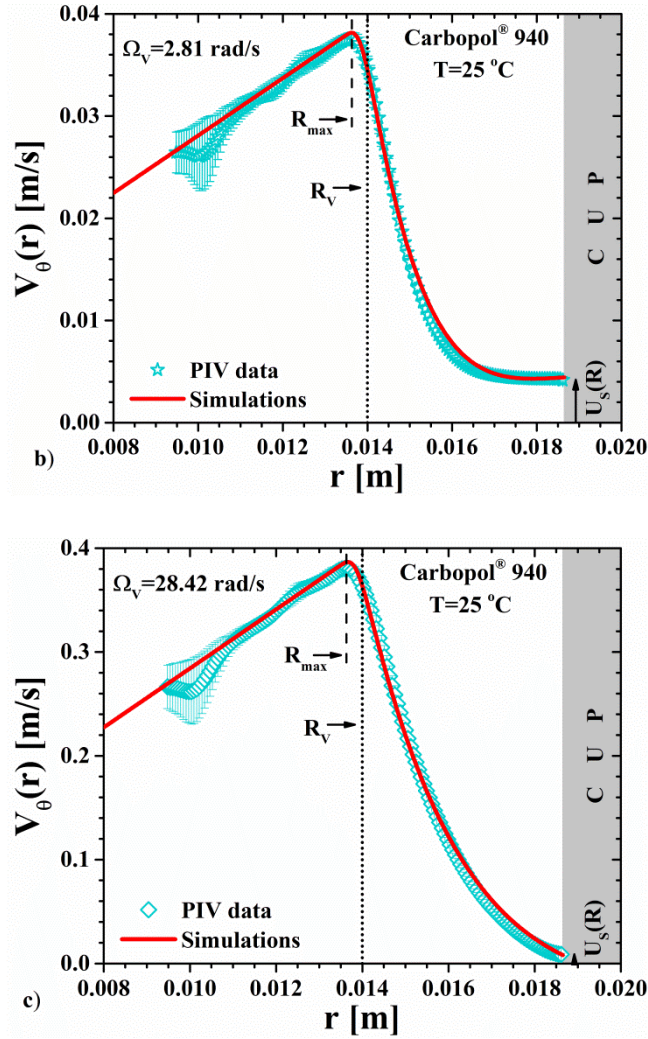
Figure 13. Tangential velocity profiles $V_\theta(r)$ extracted from the simulations shown in Fig. 12 at $\theta = 0°$ (red solid line) and PIV experiments (turquoise data points) for the Carbopol® microgel using a 24-arm fVIC geometry for various vane rotational speeds: *a) $\Omega_V = 0.047$ rad/s, b) $\Omega_V = 2.81$ rad/s; c) $\Omega_V = 28.42$ rad/s.*

Using previously-published simulation methods [33], we have simulated the steady flow of the Herschel-Bulkley fluid with wall slip to capture measurements of the fVIC geometry in Carbopol®. The material parameters and wall slip law are the same as used by Chaparian *et al.* [18]. Portions of the resulting velocity fields around the rotating vane are

shown in Figs. 12(a)-(c) for three angular speeds: $\Omega_V$ = *0.047, 2.81*, and *28.42 rad/s*. The corresponding values of the integrated torques from the surface stresses acting on the simulated fractal vane tool (as shown by the white profiled outlines in Fig. 12) are *0.482, 2.29*, and *3.750 mN m*. Because the simulation is two-dimensional (and thus represents the torque per unit length of a real vane geometry), these results must be transformed to (approximately) account for end effects to correspond to three-dimensional measured torques using the conversion Eq. (5). In this case, the conversion corresponds to equivalent 3D torques of *0.57, 2.71*, and *4.44 mN m*, respectively. These values agree well with the experimentally applied torques of *0.57, 2.56*, and *4.27 mN m*, respectively.

Radial profiles of the tangential velocity distributions, $V_\theta(r)$ (at $\theta$ = 0°) extracted from the simulation, are shown in Fig. 13 alongside experimental measurements for the microgel in the fVIC extracted from Fig 9. As we discussed earlier, for the smallest rotational speed (Fig 13(a)), the velocity increases linearly with radial distance across the entire cup, with non-zero values also measured at the outer cylinder, evidencing the existence of slip at the wall cup. As the rotational speed of the fractal vane tool increases, the material locally yields and eventually flows throughout the cup, while still slipping at the outer wall. Inspection of the simulated velocity fields in Figs. 12 and 13 shows that the location of the yield surface moves radially outwards as the imposed rotation rate increases and the relative importance of the local wall slip near the outer wall of the cup becomes less and less significant. Thus, simulations overall agree very well with PIV measurements, which further validates the use of the 24-arm fVIC geometry as a reliable rheometrical tool for a variety of complex fluids.

*III.4 Rheo-PIV of the fractal vane-in-cup flow of the κ-Carrageenan gel*

Once the *Couette analogy* and the Owens *et al.* analysis [19] have been tested for the fVIC flow of the Newtonian and simple yield-stress fluids, we have proceeded in the same manner with the aqueous κ-Carrageenan gel. This is a more complex fluid since pure κ-Carrageenan gels are thixotropic and prone to produce syneresis. A simple way to determine if a sample exhibits syneresis is to let it rest for several days and see if phase separation occurs. However, the same effect can be observed quickly when the sample is subjected to stresses, for example, in a rheometer. In such a case, segregation of the dispersing fluid at solid boundaries may also give rise to the apparent slip phenomenon. So, here we analyze the effect of syneresis on the rheological characterization of the κ-Carrageenan gel using the 24 arm fVIC flow. For this, we compare the fVIC flow with Couette and a 6-blade VIC flows and study the effect that the shearing/compressing area of the measuring geometry has on disrupting the κ-Carrageenan gel during immersion.

The torque *versus* vane rotational speed data for the κ-Carrageenan gel are included in Fig. 7. In contrast to the Carbopol® behavior, the κ-Carrageenan gel exhibited long transients in angular speed for most imposed torques (see Fig. 14), the angular speed increased with time, and in some cases a steady state was not achieved during the time of measurements. A transition in behavior appears to be occurring between the fifth and sixth torque values, *0.37* and *0.44* *mN m* (see Fig. 7), which signals the yielding of the gel. Thereafter, the rotational speeds of the vane increase significantly with the imposed torques, indicating the onset of flow and shear-thinning (or shear-banding) of the gel.
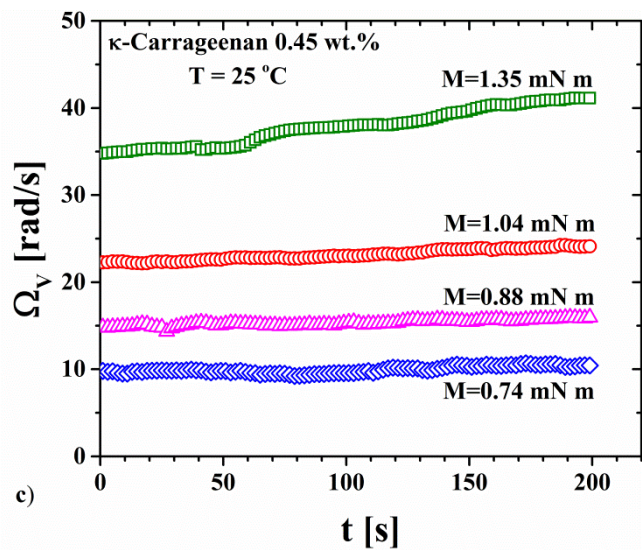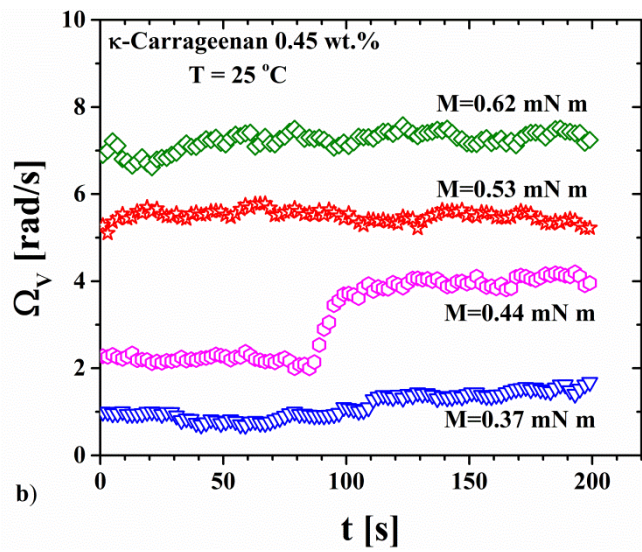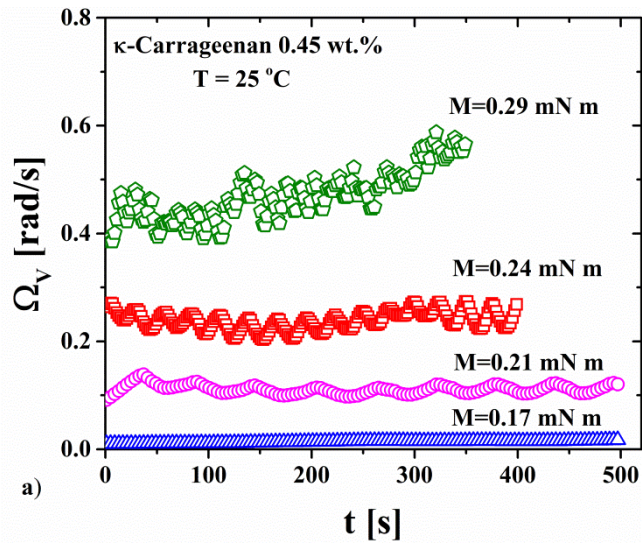
Figure 14. Evolution of $\Omega_V$ for the κ-Carrageenan gel in the 24-arm fVIC flow for different imposed torques, a) *M=0.17, 0.21, 0.24* and *0.29 mM m*; *b) M=0.37, 0.44, 0.53* and *0.62 mM m*; c) *M=0.74, 0.88, 1.04* and *1.35 mM m*.

The behavior described in Fig. 14a-c suggests a change in the microstructure of the κ-Carrageenan gel with time. To analyze such evolution in the context of thixotropic behavior, we performed a series of shear flow experiments using the 6-blade VIC covered with sandpaper *#150* to avoid slip and starting with the unperturbed gel. These experiments include up and down torque ramps with different times between points to evaluate structure breakage, as well as different resting times to test microstructure build up. For the sake of space, in Fig. 15 we present only the up and down shear rate cycles with *20 s* between points on fresh samples, followed by a resting time of *1* and *30 h*, respectively, before imposing a second up and down shear rate cycle. Clearly, there is a decrease in the viscosity of the gel with time during the first cycle, which is attributed to a change in its structure or thixotropy. Even after *30 h* at rest following a first shear rate cycle, the gel did not recover its initial structure. In this regard, it is known that once a κ-Carrageenan gel is broken, the only way to fully reform it is by heating and cooling it again, since it is a thermoreversible gel [34]. Thus, the only introduction of the fractal vane into the κ-Carrageenan gel breaks the internal structure leading to phase separation, sample inhomogeneity, and anomalous flow behavior as described below.
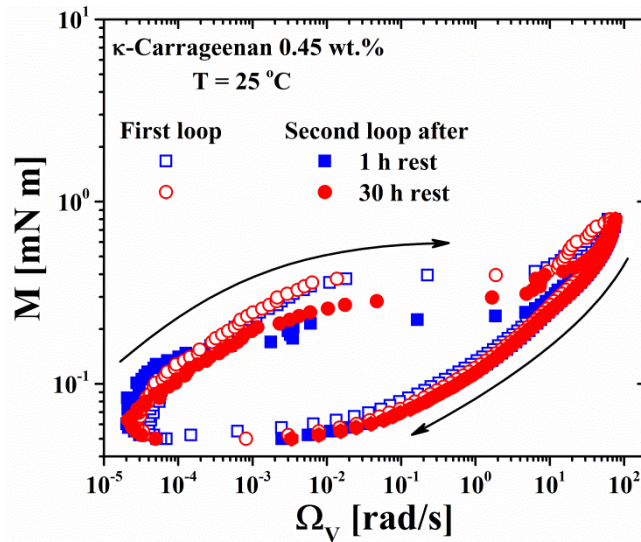
Figure 15. Up and down torque cycles with *20 s* between points: first loop with fresh sample (hollow squares) followed by a second loop after a resting time of *1 h* (filled squares); first loop with fresh sample (hollow circles) followed by a second loop after a resting time of *30 h* (filled circles), respectively, for the κ-Carrageenan gel in the 6-blade VIC flow.

The magnitude of the velocity distribution vector for the κ-Carrageenan gel in a slice (*-12°≤θ≤12°*) for the lowest (*0.44 mN m*) and highest (*1.35 mN m*) torque values with shear flow are shown in Figs. 16a and 16b, respectively. All the velocity data for this gel were obtained *100 s* after imposing the corresponding torque. It can be clearly seen that the velocity of the fluid changes with respect to $\theta$ for a given $r$, which implies that the velocity field is not axisymmetric. This result contrasts with the observations on the Carbopol® microgel, where the tangential velocity was independent of $\theta$-direction in the whole annular region (from $R_V$ to $R$).
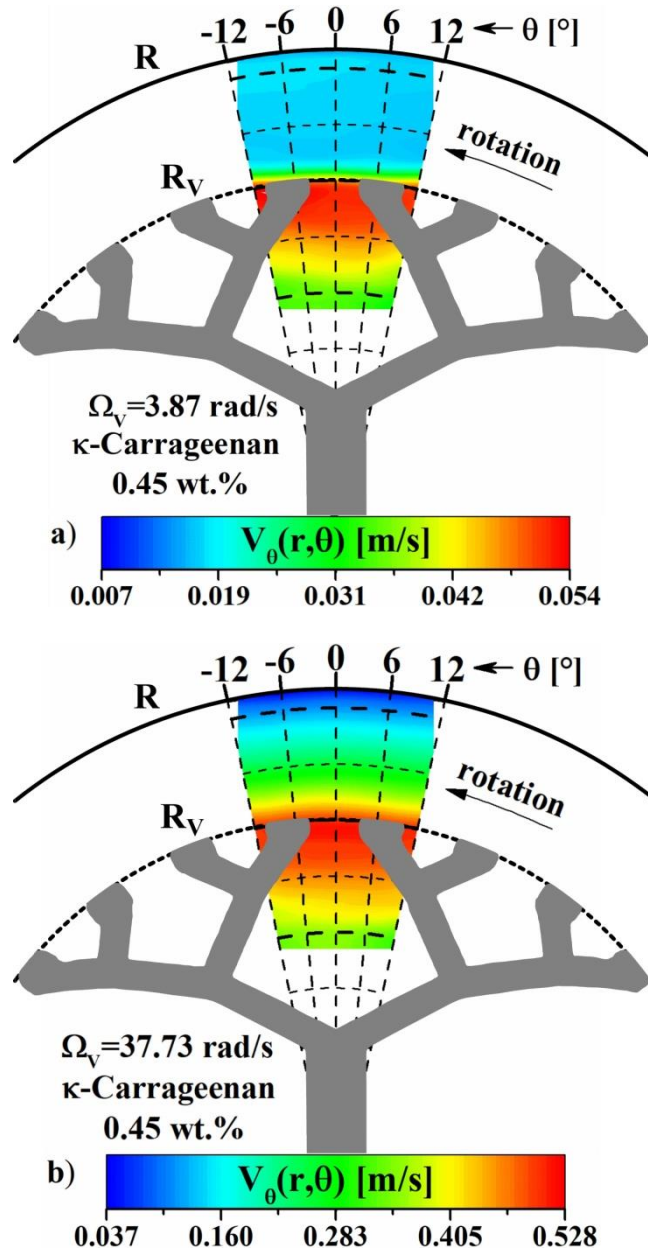
Figure 16. Magnitude of velocity distributions for the κ-Carrageenan gel in the 24-arm fVIC geometry. (a) $\Omega_V$ = 3.87 rad/s and (b) $\Omega_V$ = 37.73 rad/s. Two arms located at $\theta$ = -12° and 12°.

The velocity distributions $V_\theta(r)$ of the κ-Carrageenan gel in the fVIC flow determined using PIV at $\theta$ = 0° are shown in Figs. 17a-c for twelve torque values. At the

smallest four torques (Fig. 17a), the velocity increases linearly with radial distance in the whole flow region, indicating that the shear stress at all radial locations is smaller than the yield stress of the fluid, so that the entire gel sample undergoes rigid body-like motion. The $\Omega_V$ values determined from the velocity distributions reported in Fig. 17a (hollow symbols) match fairly well with those measured by the rheometer. The $\Omega$ values of the fluid determined from the velocity distributions reported in Fig. 17a (hollow symbols) exhibit maximum differences of *3.5, 5.5, 4.1* and *3.4%* with respect to the expected average values for $\Omega_V$=*0.013, 0.11, 0.24* and *0.43 rad/s*, respectively, measured during image acquisition. The maximum differences between these velocities were *5.5%*. Also, there are significant variations of the fluid velocity inside the vane as well as near the wall cup, in agreement with the variations described in Figs. 14a-c and 16a-b, which indicates the influence of syneresis and change in structure on the flow field. Finally, it is important to point out that the velocity distributions of the κ-Carrageenan gel also show slip at the wall cup. The slip velocity of the κ-Carrageenan gel at the glass wall cup is an increasing function of the applied torque, as shown in Fig. 18. Since the slip behavior of this gel is not relevant for the purpose of this work, we will not further discuss it here.
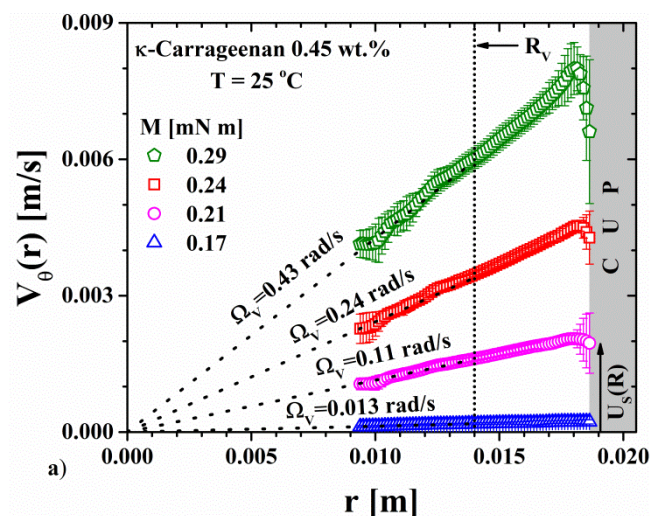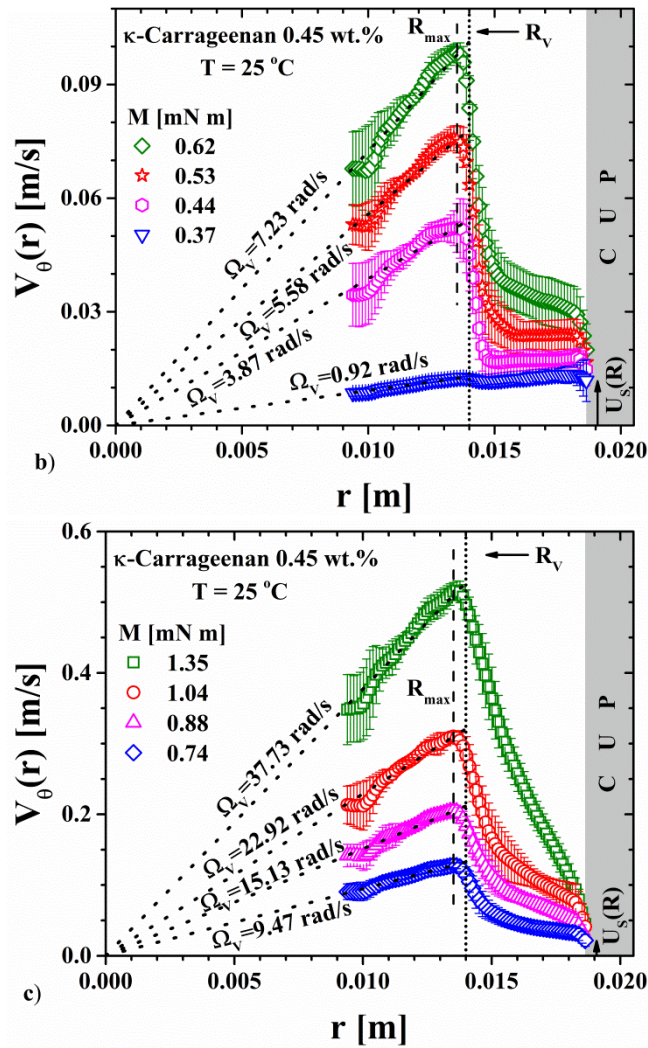
Figure 17. Velocity distributions $V_\theta(r)$, for the κ-Carrageenan gel in the 24-arm fVIC geometry at various vane rotational speeds at θ = 0°. a) $\Omega_V$= 0.013, 0.11, 0.24 and 0.43 rad/s; b) $\Omega_V$= 0.92, 3.87, 5.58 and 7.23 rad/s; c) $\Omega_V$= 9.47, 15.13, 22.92 and 37.73 rad/s. Dotted lines indicate the different vane rotational speeds.

Figures 17b-c show the velocity distributions of the κ-Carrageenan gel for $M>0.29$ mN m. Akin to the fVIC flow of the Carbopol® microgel, there are two well-defined zones in the velocity distributions of these plots, one with rigid solid-like motion and another one with shear flow and slip at the wall cup, both separated by a narrow gap between $R_{max}$ and

40

the position for the onset of flow ($R_{max} < R_V$). Again, $R_{max}$ appears independent of the applied torque (see Fig 5a). Clearly, the shape of these profiles shows that the yield stress has been surpassed. However, an outstanding characteristic of velocity distributions in Figs. 17b-c is the fact that the shear flow region does not exhibit the typical profile belonging to Couette flow [see Figs. 9b-c for example]. Instead, independently of the uncertainties in velocity measurements, Fig. 19a shows that the shear flow regions may be seen as divided into two main sub-regions, i.e., the κ-Carrageenan gel in the fVIC seems to exhibit shear banding flow [35], a fact that, to our knowledge, has not been reported for this sort of gels. Figure 19b displays the local shear rate corresponding to distributions in Fig. 19a. As can be seen, the behavior of the κ-Carrageenan gel in the fVIC flow resembles a shear banding flow [35, 36], with a region where the shear rate changes drastically near the rotating vane and another one with almost constant shear rate in most of the annular space. Moreover, another band in which the shear rate also changes rapidly is apparent close to the wall cup. It is noteworthy here that shear banding flow has been considered as characteristic of thixotropic fluids [37].

Apart from the complex flow behavior evidenced for the κ-Carrageenan gel, two additional interesting results are obtained regarding the performance of the 24-arm fVIC geometry with this gel. One is the fact that $R_{max}$ remains constant independently of flow conditions and very close to $R_V$ (see Fig. 5a), which suggests that $R_{eq}$ may be also constant for the κ-Carrageenan gel, and according to observations on the Newtonian fluid and the Carbopol® microgel, $R_{eq}$ is too expected to be closer to $R_V$ than $R_{max}$. The second and final result is that slip was not apparent around the 24-arm fractal vane in the κ-Carrageenan gel either, being these two facts relevant for rheological measurements. Thus, from the present

set of observations and results we can conclude that the 24-arm fVIC geometry can be considered as a reliable rheometrical tool for a variety of complex fluids.
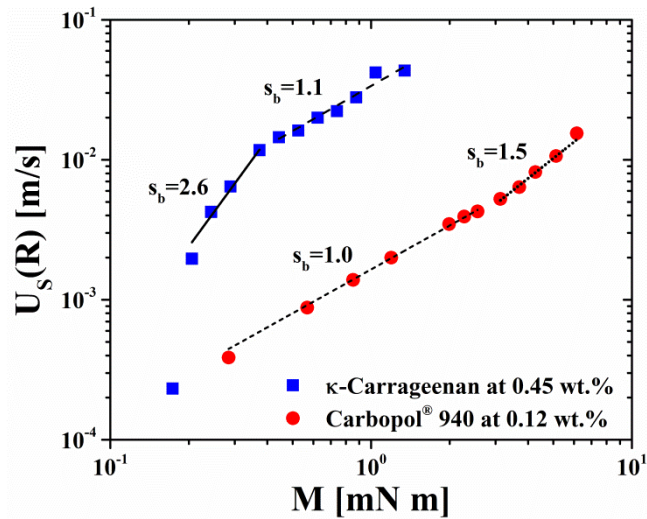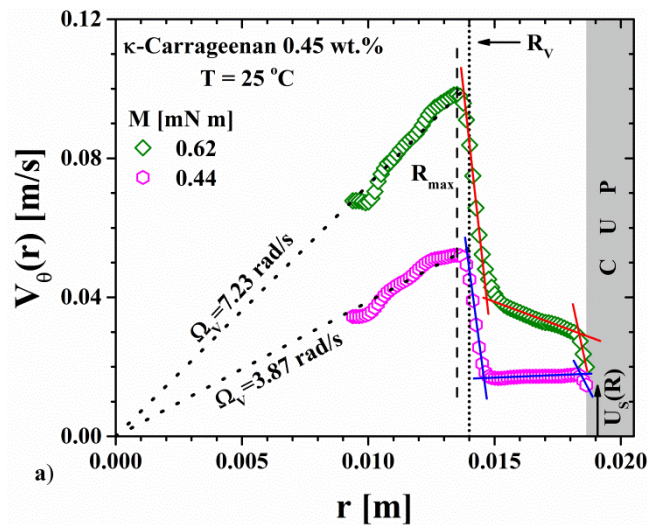


Figure 18. Slip velocity *versus* imposed torque for the Carbopol® microgel and the κ-Carrageenan gel in the 24-arm fVIC flow.
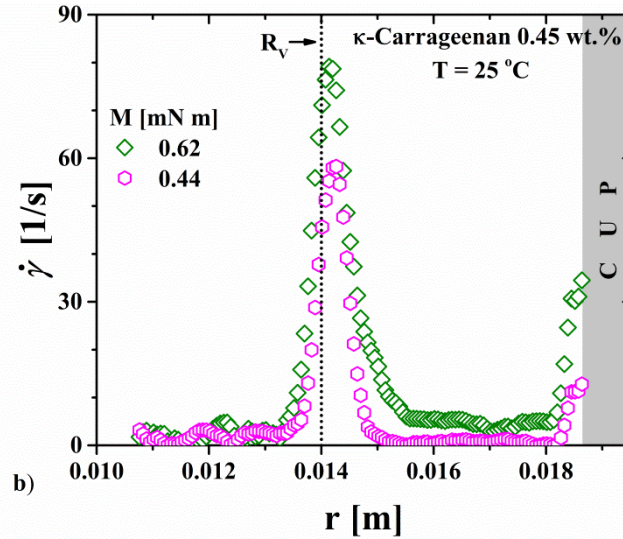
Figure 19. a) Velocity distributions, $V_\theta(r)$, for the κ-Carrageenan gel in the 24-arm fVIC geometry at θ = 0°; $\Omega_V$= *3.87* and *7.23 rad/s; b)* Shear rate distribution corresponding to velocity distributions in (a).

*III.4 Influence of the shearing/compressing area on the onset of unstable flow in the κ-Carrageenan gel*

To investigate the effect of inserting the measuring fixture on triggering the structure breakage and shear banding flow of the κ-Carrageenan gel, we have analyzed its flow behavior by two additional alternative procedures, namely, rheo-PIV in Couette and 6-blade VIC flows. Figures 20a-b show the κ-Carrageenan gel velocity distributions in Couette flow for different torque values at the bob. Note the significant variations in velocity, which correspond to unsteady measurements of the angular speed of the bob, akin to those in Fig. 14. Despite these large oscillations, different shear bands also appear fairly well defined. This similitude of the fVIC and Couette flow behavior of the κ-Carrageenan gel can be explained by the fact that, as already shown above, the flow field of the 24-arm fVIC approaches to the Couette one very much. Again, it is suggested that the only

introduction of the bob into the κ-Carrageenan gel accelerates the phase separation and structure breakage that lead to shear banding.
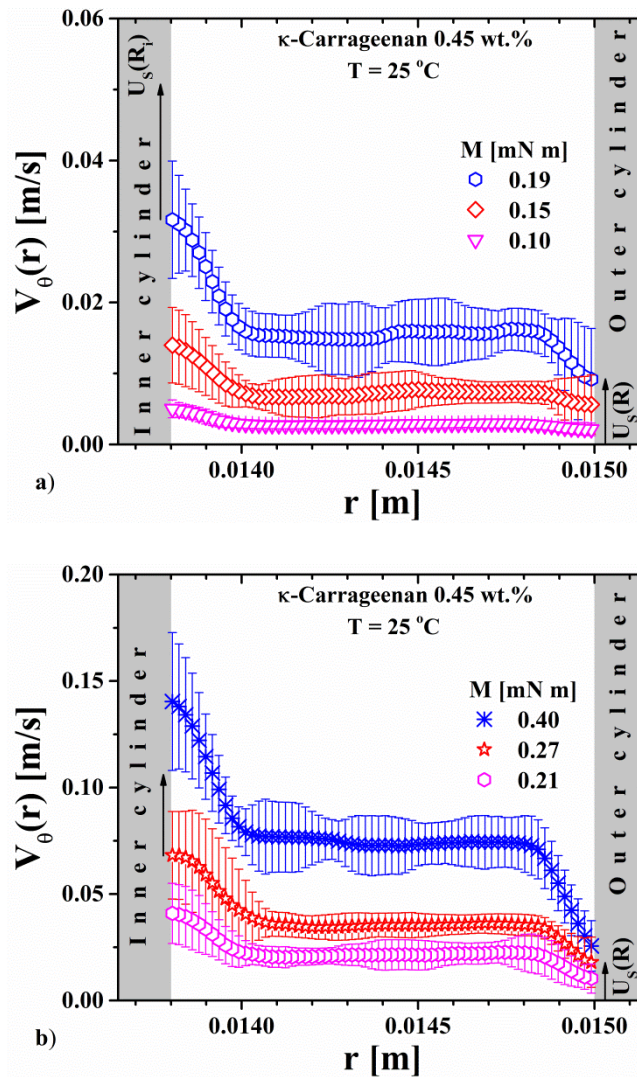


Figure 20. Velocity distributions $V_\theta(r)$, for the κ-Carrageenan gel in the Couette cell at various torques at $\theta = 0°$. a) $M= 0.10, 0.15$ and $0.19$ mN m; b) $M= 0.21, 0.27$ and $0.40$ mN m.

Finally, Figs. 21a-b exhibit the velocity distributions of κ-Carrageenan gel in the 6-blade VIC flow. Again, variations of the velocity occur as in the 24-arm fVIC and

Couette geometries. Yet, contrasting with the other two geometries, the average velocity distributions in the 6-blade VIC conform to those observed for a "well-behaved" gel, as the Carbopol® microgel with slip at the cup [7], that is, shear banding is not apparent. Unfortunately, the variations in velocity distributions are still large to try to construct a reliable flow curve for the κ-Carrageenan gel. Thus, from the analysis of the κ-Carrageenan gel using different geometries, it is clear that the geometry used has an impact on the gel structure. We can state that the shearing/compression of the sample during the introduction of the measuring geometry (24-arm fractal vane and bob) accelerates phase separation in the fluid, which leads to anomalous flow behavior. On the other hand, the 6-blade vane introduces much more limited distortion into the sample and seems to eliminate the anomalous behavior. Despite this fact, this vane does not permit a reliable rheological characterization either. Clearly, the area in contact with the fluid, which is able to stress/compress the sample, is critical in the process. Table 3 shows the OAF calculated for various cruciform/fractal vanes (with the same diameter and thickness) as compared to an equivalent solid bob, and the area occluded by the vane as compared to the corresponding area of a vane with N-straight blades (denoted $AOF_N$). The OAF has the same numerical value as the corresponding volume ratio [19]. Note that convergence of blades in the center of a standard vane results in an increase in OAF. Also, videos in the supplemental material (Fig. 22a-c) of the insertion of the cylinder, 24-arm fractal vane and 6-blade standard vane, respectively, into the κ-Carrageenan gel (as seen between crossed polarizers) exhibit the extent to which the gel is deformed by each fixture.

In this set of tests, the OAF has the following trend: $OAF_{Couette} > OAF_{FV} > OAF_{6\ blade\ vane}$, which explains the observed behavior. Hence, an obvious objective to widen the range of applications of fractal vanes is to minimize the OAF while approaching to the ideal

45

Couette-like behavior. ==Thus, according to Table 3 and based on recent simulations [18] and experiments with foams [20], a 12-arm fractal vane might be a good candidate to achieve this goal, the fact, however, remains to be tested.==
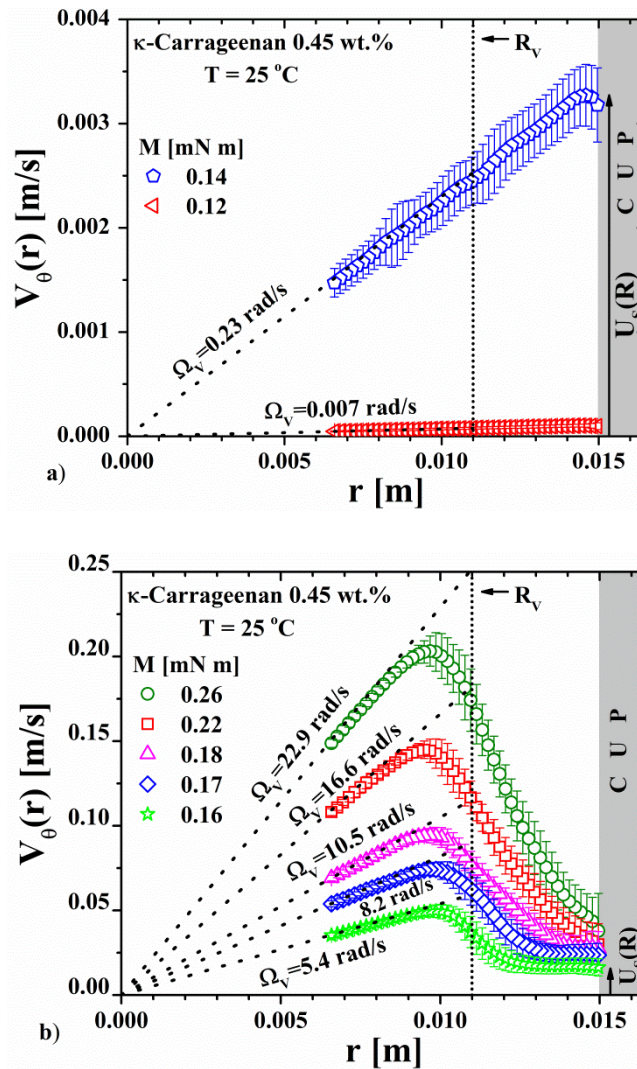


Figure 21. Velocity distributions, $V_\theta(r)$, for the κ-Carrageenan gel in the 6-blade VIC geometry at $\theta = 0°$ and various rotational speeds; a) $\Omega_V = 0.007$ and $0.23$ rad/s; b) $\Omega_V = 5.4$, $8.2$, $10.5$, $16.6$ and $22.9$ rad/s. Dotted lines indicate the different vane rotational speeds.
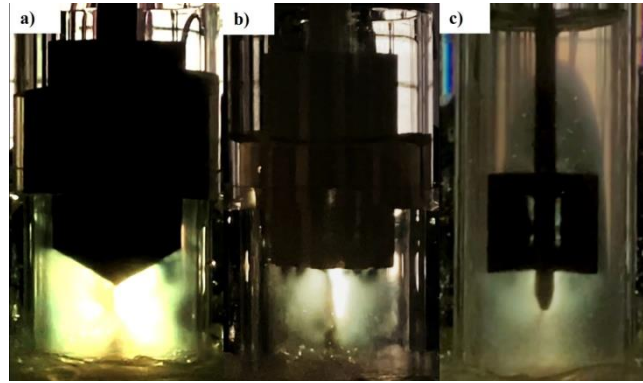
Figure 22. Immersion of fixtures into a cup with κ-Carrageenan gel as seen between crossed polarizers, a) solid cylinder "Multimedia view"; b) 24-arm fractal vane "Multimedia view"; c) 6-blade vane "Multimedia view".

Table 3. Occluded area fraction (OAF) of various cruciform/fractal vanes as compared to an equivalent solid bob, and area occluded by the vane as compared to the corresponding area of a vane with N-straight arms (denoted $AOF_N$). The OAF has the same numerical value as the corresponding volume ratio.

| | | | | | | |
|---|---|---|---|---|---|---|
| Type | Vane | Vane | Vane | Fractal | Fractal | Cylinder |
| Arms | N=6 | 12 | 24 | 12 | 24 | →∞ |
| OAF | 0.15 | 0.27 | 0.50 | 0.22 | 0.30 | 1.00 |
| $OAF_N$ | 1.00 | 1.00 | 1.00 | 0.83 | 0.60 | 1.00 |

## CONCLUSIONS

The flow field of a Newtonian fluid, a non-thixotropic Carbopol® 940 microgel, and a thixotropic κ-Carrageenan gel around a 3D printed fVIC geometry was analyzed in this work by means of Rheo-PIV. For the Newtonian fluid and the microgel, PIV measurements showed that the fractal vane produces rigid body-like motion for almost all the fluid in between the vane arms, as well as axisymmetric flow field in the annular gap out to the

bounding wall of the cup. Simulations of the fVIC flow of the microgel with slip at the wall cup agree very well with PIV velocity distributions. Overall, it is found that for both the Newtonian fluid and the model microgel, the effective shearing radius of the fractal vane fixture, $R_{eq}$, remains constant, allowing the use of the *Couette analogy* and the Owens *et al.* [19] analysis, both with outstanding accuracy. Thus, the present set of results validates the 24-arm fVIC geometry as a reliable rheometrical tool for a variety of complex fluids.

On the other hand, the only immersion of the measuring geometries into the κ-Carrageenan gel accelerates the onset of syneresis, which results in shear banding for both the Couette and fVIC flows. This disturbance of the sample during rheometrical fixture immersion is attributed to shearing/compression of the sample and cannot be avoided regardless of specific geometric fixtures. By comparing results obtained using the 24-arm fVIC geometry with other conventional geometries, Couette and 6-blade VIC, we investigated the effect that the shearing/compressing area of the measuring geometry has on disrupting the κ-Carrageenan gel during its insertion. We show that the OAF, which is able to stress/compress the sample, is critical in the process. Decreasing the OAF limits the appearance of the shear-banding instability in the κ-Carrageenan gel. Thus, an obvious objective to widen the range of applications of fractal vanes is to minimize OAF while approaching to the ideal Couette-like behavior. In this sense, a 12-arm fractal vane might be a good candidate to achieve this goal.

**ACKNOWLEDGMENTS**

**APPENDIX A:** *Rheometrical characterization of the κ-Carrageenan gel*

Despite the high sensitivity of the κ-Carrageenan gel to shear/compression and syneresis that result in unstable flow, we carried out a basic rheometrical characterization of the gel (with and without tracer particles) under dynamic oscillatory and transient shear flow by using a parallel-plate geometry (50 mm in diameter) clean and covered with sandpaper *#150* to prevent slip, as well as with a clean Couette cell. Figures 23a-b display the storage ($G'$) and loss modulus ($G''$) of the gel measured as functions of the angular frequency for an oscillating stress of 0.5 Pa. In both cases, data obtained with and without sandpaper on the plates, the moduli are relatively independent of frequency and $G' >> G''$ indicating a characteristic gel-like behavior. Also, it can be seen that the tracer particles do not affect the rheological behavior of the samples and that the elastic modulus seems to increase in the presence of slip (plates without sandpaper, see [39]). Finally, the ratio $G'/G'' \sim 10$ indicates that κ-Carrageenan produces strong gels.
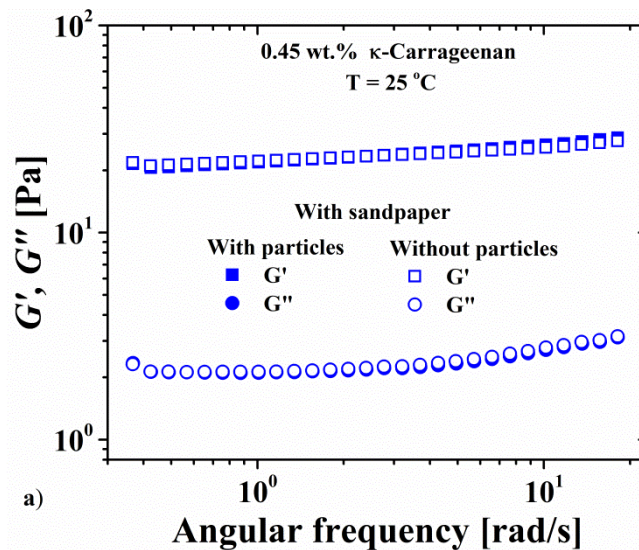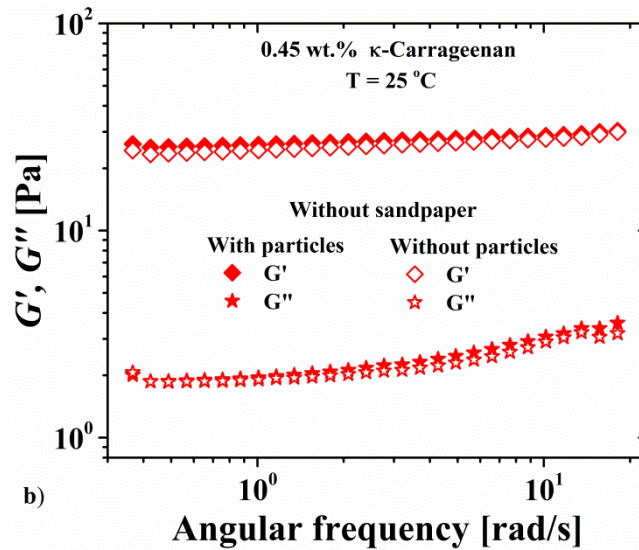
Figure 23. *G'* and *G''* as functions of the angular frequency for the κ-Carrageenan gel in parallel-plate, a) with sandpaper, b) without sandpaper.

Figure 24 shows a series of apparent flow curves obtained for the κ-Carrageenan gel using parallel-plates covered with and without sandpaper as well as with two clean Couette cells (*k=0.92* and *0.75*) for the purpose of comparison. Since the sample is thixotropic and the flow is mostly unstable (see section III.4), we chose a time of 30 s between consecutive points to gather the flow data in an up ramp, in other words, we measured a transient flow curve only to be used as reference. It can be seen that the flow curves obtained with the clean parallel-plate and Couette geometries are comparable in shape and affected by slip, as seen from comparison with the flow curve obtained with sandpaper covered parallel-plates. Note that the Couette cells with different *k*-ratio result in different flow curves, presumably due to different shearing/compression history of the sample during insertion. Finally, the flow curve obtained with sandpaper covered parallel-plates exhibits a sudden jump in shear rate at about 20 Pa, which may be indicative of the onset of shear banding [38].
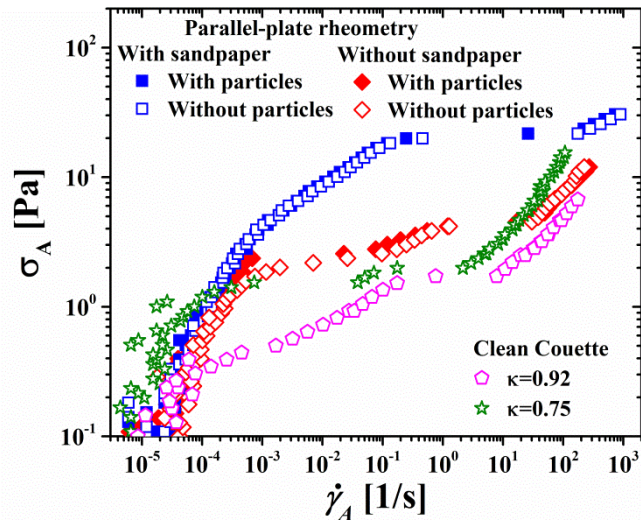
Figure 24. Apparent flow curves obtained for the κ-Carrageenan gel using parallel-plate covered with and without sandpaper as well as with two clean Couette cells ($k=0.92$ and $0.75$).

**REFERENCES**

[1] Flodin, N., and B. Broms, "Historical development of civil engineering in soft clay," in Soft Clay Engineering (Development in geotechnical engineering), Ed. E. W. Brand and R. P. Brenner (Elsevier Amsterdam, The Netherlands, 1981) Vol. 20.

[2] Dzuy, N. Q., and D. V. Boger, "Yield stress measurement for concentrated suspensions", J. Rheol. **27**, 321-349 (1983). https://doi.org/10.1122/1.549709.

[3] Barnes, H. A., and J. O. Carnali, "The vane-in-cup as a novel rheometer geometry for shear thinning and thixotropic materials," J. Rheol. **36**, 841-866 (1990). https://doi.org/10.1122/1.550103.

[4] Bousmina, M., A. Aït-Kadi, and J. B. Faisant, "Determination of shear rate and viscosity from batch mixer data," J. Rheol. **43**, 415-433 (1999). https://doi.org/10.1122/1.551044.

[5] Aït-Kadi, A., P. Marchal, L. Choplin, A.-S. Chrissemant, and M. Bousmina, "Quantitative Analysis of Mixer-Type Rheometers using the *Couette analogy*," Can. J. Chem. Eng. **80**, 1166-1174 (2002). https://doi.org/10.1002/cjce.5450800618.

[6] Estellé, P., C. Lanos, A. Perrot, and S. Amziane, "Processing the vane shear flow data from *Couette analogy*," Appl. Rheol. 18, 34037-34481 (2008). https://doi.org/10.1515/arh-2008-0009.

[7] Medina-Bañuelos, E. F., B. M. Marín-Santibáñez, J. Pérez-González, and D. M. Kalyon, "Rheo-PIV analysis of the vane in cup flow of a viscoplastic microgel," J. Rheol. **63**, 905-915 (2019). https://doi.org/10.1122/1.5118900.

[8] Atkinson, C., and J. D. Sherwood, "The torque on a rotating n-bladed vane in a Newtonian fluid or linear elastic medium," Proc. R. Soc. A Math. Phys. Eng. Sci. **438**, 183–196 (1992). https://doi.org/10.1098/rspa.1992.0101.

[9] Sherwood, J. D., and G. H. Meeten, "The use of the vane to measure the shear modulus of linear elastic solids," J. Nonnewton. Fluid Mech. **41**, 101–118 (1991). https://doi.org/10.1016/0377-0257(91)87037-X.

[10] Potanin, A., "3D simulations of the flow of thixotropic fluids, in large gap Couette and vane-cup geometries," J. Nonnewton. Fluid Mech. **165**, 299–312 (2010). https://doi.org/10.1016/j.jnnfm.2010.01.004.

[11] Keentok, M., J. F. Milthorpe, and E. O'Donovan, "On the shearing zone around rotating vanes in plastic liquids: Theory and experiment," J. Non-Newt. Fluid Mech. **17**, 23-35 (1985). https://doi.org/10.1016/0377-0257(85)80003-3.

[12] Baravian, C., A. Lalante, and A. Parker, "Vane rheometry with a large, finite gap," Appl. Rheol. **12**, 81-87 (2002). https://doi.org/10.1515/arh-2002-0005.

[13] Savarmand, S., M. Heniche, V. Béchard, F. Bertrand, and P. J. Carreau, "Analysis of the vane rheometer using 3D finite element simulation," J. Rheol. **51**, 161-177 (2007). https://doi.org/10.1122/1.2433936.

[14] Zhu, H., N. S. Martys, C. Ferraris, and D. De Kee, "A numerical study of the flow of Bingham-like fluids in two-dimensional vane and cylinder rheometers using a smoothed particle hydrodynamics (SPH) based method," J. Non-Newtonian Fluid Mech. **165**, 362-375 (2010). https://doi.org/10.1016/j.jnnfm.2010.01.012.

[15] Ovarlez, G., F. Mahaut, F. Bertrand, and X. Chateau, "Flows and heterogeneities with a vane tool: MRI measurements," J. Rheol. **55**, 197-223 (2011). https://doi.org/10.1122/1.3526349.

[16] Nazari, B., R. H. Moghaddam, and D. Bousfield, "A three-dimensional model of a vane rheometer," Int. J. Heat Fluid Fl. **42**, 289-295 (2013). https://doi.org/10.1016/j.ijheatfluidflow.2013.02.012.

[17] Marchesini, F. H., M. F. Naccache, A. Abdu, A. A. Alicke, P. R. de Souza Mendes, "Rheological characterization of yield-stress materials: Flow pattern and apparent wall slip," Appl. Rheol. **25**, 53883 (2015). https://doi.org/10.3933/applrheol-25-53883.

[18] Chaparian, E., C. E. Owens, and G. H. McKinley, "Computational rheometry of yielding and viscoplastic flow in vane-and-cup rheometer fixtures," Manuscript submitted to J. Non-Newtonian Fluid Mech. (2022). https://doi.org/10.48550/arXiv.2202.04255.

[19] Owens, C., A. J. Hart, and G. H. McKinley "Improved rheometry of yield stress fluids using bespoke fractal 3D printed vanes," J. Rheol. **64**, 643-662 (2019). https://doi.org/10.1122/1.5132340.

[20] Carraretto, I. M., C. E. Owens, and G. H. McKinley, "Time-resolved rheometry of coarsening foams using three dimensionally printed fractal vanes," Phys. Fluids **34**, 113108 (2022). https://doi.org/10.1063/5.0119944.

[21] Ovarlez, G., S. Cohen-Addad, K. Krishan, J. Goyon, and P. Coussot, "On the existence of a simple yield stress fluid behavior," J. Non-Newtonian Fluid Mech. **193**, 68-79 (2013). http://dx.doi.org/10.1016/j.jnnfm.2012.06.009

[22] Ramakrishnan, S., C. G. Gerardin, and R. K. Prud'homme, "Syneresis of Carrageenan Gels: NMR and Rheology," Soft Materials **2**, 145-153 (2004). https://doi.org/10.1081/SMTS-200056119.

[23] Medina-Bañuelos, E. F., B. M. Marín-Santibáñez, J. Pérez-González, M. Malik, and D. M. Kalyon, "Tangential annular (Couette) flow of a viscoplastic microgel with wall slip," J. Rheol. **61**, 1007-1022 (2017a). https://doi.org/10.1122/1.4998177.

[24] Medina-Bañuelos, E. F., B. M. Marín-Santibáñez, J. Pérez-González, and F. Rodríguez-González, "Couette Flow of a yield-stress fluid with slip as studied by Rheo-PIV," Appl. Rheol. **27**, 53893 (2017b). http://doi.org/10.3933/ApplRheol-27-53893.

[25] Medina-Bañuelos, E. F., B. M. Marín-Santibáñez, J. Pérez-González, and F. Rodríguez-González "Rheo-PIV analysis of the steady torsional parallel-plate flow of a viscoplastic microgel with wall slip," J. Rheol. **66**, 31-48 (2022). https://doi.org/10.1122/8.0000310.

[26] Rinaudo, M., "Seaweed Polysaccharides" in Comprehensive Glycoscience, Ed: Hans Kamerling (Elsevier, 2007), Vol. 2, 691-735, ISBN 9780444519672, https://doi.org/10.1016/B978-044451967-2/00140-9.

[27] Macosko, C. W., Rheology: Principles, measurements, and applications (WILEY-VCH, New York, 1994).

[28] Kalyon, D. M., "Apparent slip and viscoplasticity of concentrated suspensions," J. Rheol. 49, 621-640 (2005). https://doi.org/10.1122/1.1879043.

[29] Kalyon, D. M., and S. Aktaş, "Factors affecting the rheology and processability of highly filled suspensions," Annual Rev. Chem. Biomol. Eng **5**, 229-254 (2014). https://doi.org/10.1146/annurev-chembioeng-060713-040211.

[30] Aktas, S., D. M. Kalyon, B. M. Marín-Santibáñez and J. Pérez-González, "Shear viscosity and wall slip behavior of a viscoplastic hydrogel", J. Rheol. **58**, 2, 513-535 (2014). https://doi.org/10.1122/1.4866295.

[31] Meeker, S. P., R. T. Bonnecaze, and M. Cloitre, "Slip and flow in pastes of soft particles: Direct observation and rheology," J. Rheol. **48**, 1295-1320 (2004a). https://doi.org/10.1122/1.1795171.

[32] Meeker, S. P., R. T. Bonnecaze, and M. Cloitre, "Slip and Flow in Soft Particle Pastes," Phys. Rev. Lett. **92**, 198302 (2004b). https://doi.org/10.1103/PhysRevLett.92.198302.

[33] Chaparian, E., and O. Tammisola, "Sliding flows of yield-stress fluids," J. Fluid Mech. **911**, A17 (2021). https://doi.org/10.1017/jfm.2020.1014

[34] Phillips, C. O., and P. A. Williams, Handbook of hydrocolloids (WOODHEAD PUBLISHING LIMITED, Cambridge, 2009).

[35] Divoux, T., M. A. Fardin, S. Manneville, and S. Lerouge, "Shear banding of complex fluids," Ann. Rev. Fluid Mech. **48**, 81-103 (2016). https://doi.org/10.1146/annurev-fluid-122414-034416.

[36] Marín-Santibáñez, B. M., J. Pérez-González, and F. Rodríguez-González, "Origin of shear thickening in semidilute wormlike micellar solutions and evidence of elastic turbulence," J. Rheol. **58**, 1917-1933 (2014). https://doi.org/10.1122/1.4897267.

[37] Larson, R. G., and Y. Wei, A review of thixotropy and its rheological modeling, J. Rheol. **63**, 477-501 (2019). https://doi.org/10.1122/1.5055031.

[38] Méndez-Sánchez, A. F., J. Pérez-González, L. de Vargas, J. R. Castrejón-Pita, A. A. Casterjón-Pita, and G. Huelsz, "Particle image velocimetry of the unstable capillary flow of a micelar solution", J. Rheol. **47**, 1455-1466 (2003). http://dx.doi.org/10.1122/1.1621421

[39] Ortega-Avila, J. F., J. Pérez-González, B. M. Marín-Santibáñez, F. Rodríguez-González, S. Aktas, M. Malik, and D. M. Kalyon, "Axial annular flow of a viscoplastic microgel with wall slip", J. Rheol. **60**, 503-515 (2016). http://dx.doi.org/10.1122/1.4945820.

**Captions for figures**

**Figure 1.** The 3D printed fractal vane and its coupling to the UDS 200 rheometer.

**Figure 2.** Experimental set-up for the rheo-PIV measurements with the 24-arm fVIC geometry.

**Figure 3.** ROI for PIV measurements and zoom of the velocity map in the 24-arm fVIC flow.

**Figure 4.** Velocity distributions, $V_\theta(r)$, in the 24-arm fVIC geometry for the Newtonian fluid, glycerol, determined with the PIV method for six vane rotational speeds. (a) $\Omega_V$ = *1.1, 2.22* and *4.48 rad/s* and (b) $\Omega_V$ = *9.06, 13.88* and *18.89 rad/s.* c) Normalized velocity distributions for different torque values. Dotted lines indicate the different vane rotational speeds. Continuous lines indicate the theoretical velocity profiles, i.e., Eq. (1), for *$R_{eq}$= 13.87 mm*.

**Figure 5.** a) $R_{max}/R_V$ *versus* $M/M_{max}$ for glycerol, and Carbopol® and κ-Carrageenan gels in the 24-arm fVIC geometry, as well as for glycerol and Carbopol® microgel in the 6-blade VIC geometry. b) $R_{eq}/R_V$ *versus* $M/M_{max}$ for glycerol and Carbopol® microgel in the 24-arm fVIC geometry, as well as for glycerol and Carbopol® microgel in the 6-blade VIC geometry. The dashed and continuous vertical red lines indicate the ratio of torque at yielding, $M_y$, and the maximum imposed torque, $M_{max}$, $M_y/ M_{max}$, for the Carbopol® microgel in the 24-arm fVIC and 6-blade VIC, respectively. Data for glycerol and Carbopol® microgel in the 6-blade VIC flow are reproduced from [7].

**Figure 6.** Flow and viscosity curves for glycerol using different methods.

**Figure 7.** Torque *versus* rotational speed curves for the Carbopol® and κ-Carrageenan gels in the 24-arm fVIC flow. Carbopol® microgel data are steady, while those of the κ-Carrageenan gel data were collected *100 s* after torque imposition.

**Figure 8.** Magnitude of velocity distributions under steady state for the Carbopol® microgel in the 24-arm fVIC geometry. (a) $\Omega_V$ = *1.35 rad/s* and (b) $\Omega_V$ = *51.77 rad/s*. Two arms located at $\theta$ = *-12° and 12°*.

**Figure 9.** Velocity distributions $V_\theta(r)$, for the Carbopol® microgel in the 24-arm fVIC geometry at various vane rotational speeds at $\theta$ = 0°. *a) $\Omega_V$= 0.021, 0.047, 0.075* and *0.11 rad/s; b) $\Omega_V$= 0.57, 1.35* and *2.81 rad/s; c) $\Omega_V$= 7.93, 16.28, 51.77* and *83.87 rad/s*. Dotted lines indicate the different vane rotational speeds. Continuous lines indicate the theoretical profiles calculated with Eqs. (7) and (8).

**Figure 10.** Schematic representation of the annular flow region in a Couette cell showing the three possible flow regimes in the presence of slip at wall cup, namely, (I) pure plug flow in the entire gap for $\sigma_{r\theta}(kR) < \sigma_y$, (II) shear flow for $kR \leq r < R_y$ ($\sigma_{r\theta}(kR) \geq \sigma_{r\theta}(r) \geq \sigma_y$) and plug flow for $R_y \leq r \leq R$ ($\sigma_y > \sigma_{r\theta}(r) \geq \sigma_{r\theta}(R)$), finally, pure shear flow for $\sigma_{r\theta}(R) > \sigma_y$ (III).

**Figure 11.** Flow curve of the Carbopol® microgel obtained using different methods. Parallel-plate with sandpaper data are reproduced from [25].

**Figure 12.** Results from steady numerical simulations with the Hershel-Bulkley model showing the magnitude of the velocity distribution (in [m/s]) for the Carbopol® microgel in the 24-arm fVIC geometry below yielding at (a) $\Omega_V$ = *0.047 rad/s*, and after yielding at (b) $\Omega_V$ = 2.81 *rad/s* and (c) $\Omega_V$ = *28.42 rad/s*.

**Figure 13.** Tangential velocity profiles $V_\theta(r)$ extracted from the simulations shown in Fig. 12 at $\theta$ = *0°* (red solid line) and PIV experiments (turquoise data points) for the Carbopol®

microgel using a 24-arm fVIC geometry for various vane rotational speeds: *a)* $\Omega_V$= *0.047 rad/s, b)* $\Omega_V$=*2.81 rad/s*; *c)* $\Omega_V$= *28.42 rad/s*.

**Figure 14.** Evolution of $\Omega_V$ for the κ-Carrageenan gel in the 24-arm fVIC flow for different imposed torques, a) *M=0.17, 0.21, 0.24* and *0.29 mM m*; *b) M=0.37, 0.44, 0.53* and *0.62 mM m*; c) *M=0.74, 0.88, 1.04* and *1.35 mM m*.

**Figure 15.** Up and down torque cycles with *20 s* between points: first loop with fresh sample (hollow squares) followed by a second loop after a resting time of *1 h* (filled squares); first loop with fresh sample (hollow circles) followed by a second loop after a resting time of *30 h* (filled circles), respectively, for the κ-Carrageenan gel in the 6-blade VIC flow.

**Figure 16.** Magnitude of velocity distributions for the κ-Carrageenan gel in the 24-arm fVIC geometry. (a) $\Omega_V$ = *3.87 rad/s* and (b) $\Omega_V$ = *37.73 rad/s*. Two arms located at $\theta$ = *-12° and 12°*.

**Figure 17.** Velocity distributions $V_\theta(r)$, for the κ-Carrageenan gel in the 24-arm fVIC geometry at various vane rotational speeds at $\theta$ = 0°. a) $\Omega_V$= *0.013, 0.11, 0.24* and *0.43 rad/s; b)* $\Omega_V$= *0.92, 3.87, 5.58* and *7.23 rad/s*; *c)* $\Omega_V$= *9.47, 15.13, 22.92* and *37.73 rad/s*. Dotted lines indicate the different vane rotational speeds.

**Figure 18.** Slip velocity *versus* imposed torque for the Carbopol® microgel and the κ-Carrageenan gel in the 24-arm fVIC flow.

**Figure 19.** a) Velocity distributions, $V_\theta(r)$, for the κ-Carrageenan gel in the 24-arm fVIC geometry at $\theta$ = 0°; $\Omega_V$= *3.87* and *7.23 rad/s; b)* Shear rate distribution corresponding to velocity distributions in (a).

**Figure 20.** Velocity distributions $V_\theta(r)$, for the κ-Carrageenan gel in the Couette cell at various torques at θ = 0°. a) *M= 0.10, 0.15* and *0.19 mN m; b) M= 0.21, 0.27* and *0.40 mN m*.

**Figure 21.** Velocity distributions, $V_\theta(r)$, for the κ-Carrageenan gel in the 6-blade VIC geometry at *θ = 0°* and various rotational speeds; a) *Ω_V= 0.007* and *0.23 rad/s; b) Ω_V= 5.4, 8.2, 10.5, 16.6* and *22.9 rad/s*. Dotted lines indicate the different vane rotational speeds.

**Figure 22.** Immersion of fixtures into a cup with κ-Carrageenan gel as seen between crossed polarizers, a) solid cylinder "Multimedia view"; b) 24-arm fractal vane "Multimedia view"; c) 6-blade vane "Multimedia view".

**Figure 23.** *G'* and *G''* as functions of the angular frequency for the κ-Carrageenan gel in parallel-plate, a) with sandpaper, b) without sandpaper.

**Figure 24.** Apparent flow curves obtained for the κ-Carrageenan gel using parallel-plate covered with and without sandpaper as well as with two clean Couette cells (*k=0.92* and *0.75*).